An in-depth comparative FEA on through-thickness residual stresses in press-braked cold-formed steel section

Ayad Mutafi [a], J.M. Irwan [a,*], Noorfaizal Yidris [b], Atef M. Ghaleb [c,**], Sami Al-Alimi [d,***],
Mugahed Amran [e], Maged Qasem [f], Mousa Hasan [f], Amin Al-Fakih [g,h]

[a] Jamilus Research Centre for Sustainable Construction (JRC-SC), Faculty of Civil Engineering and Built Environment, Universiti Tun Hussein Onn Malaysia, Parit Raja, 86400, Johor, Malaysia
[b] Department of Aerospace Engineering, Universiti Putra Malaysia, Selangor, Malaysia
[c] Department of Industrial Engineering, College of Engineering, Alfaisal University, 11533, Riyadh, Saudi Arabia
[d] Sustainable Manufacturing and Recycling Technology, Advanced Manufacturing and Materials Center (SMART-AMMC), Universiti Tun Hussein Onn Malaysia (UTHM), Parit Raja, 86400, Malaysia
[e] Department of Civil Engineering, College of Engineering, Prince Sattam Bin Abdulaziz University, Alkharj, 16273, Saudi Arabia
[f] Department of Engineering, Razak Faculty of Technology and Informatics, University Technology Malaysia, Kuala Lumpur, 54100, Malaysia
[g] Department of Civil and Environmental Engineering, King Fahd University of Petroleum & Minerals, Dhahran 31261, Saudi Arabia
[h] Interdisciplinary Research Center for Construction and Building Materials, King Fahd University of Petroleum & Minerals, Dhahran 31261, Saudi Arabia

A R T I C L E   I N F O

A B S T R A C T

The finite element (FE) is one of the techniques implemented to predict residual stresses. The selection of the proper FE technique is essential to achieve accurate results. This study investigated the prediction of residual stress distribution in pressed-braked thin-walled cold-formed steel sections using the 3D-Shell finite element (FE) technique. Cold-forming processes produce residual stresses and affect the structural capacity of thin-walled cold-formed steel sections. Previous studies have used and recommended the 3D-Solid FE technique to predict residual stresses; however, limited studies have applied this 3D-Shell FE technique. Therefore, the results showed this study had compared the longitudinal/transverse residual stresses and the neutral axis shift obtained by the 3D-Shell FE technique with the results from the literature using the 3D-Solid FE technique. It is also revealed that there are limitations in the 3D-Shell FE technique for predicting residual stresses.

1. Introduction

Computational analysis of technical problems has taken great strides over the last few decades with advancements in computational tools. Thanks to its efficiency and cost-saving, numerical simulation is one of the key tools in science and industrial engineering problems. Numerical simulation of sheet metal formation began in the 1990s. Thus far, different modeling techniques have been used for sheet metal forming.

According to Ablat & Qattawi [1], the finite element method (FEM) is widely implemented in sheet metal formation simulations. Based on their review, many researchers preferred FEM over the other numerical simulations due to its efficiency and accuracy. In FEM, different solution strategies and formulations are applied Makinouchi, 1996 [2]. More-over, in sheet metal forming, static implicit and dynamic explicit are the

solution strategies that many researchers have extensively implemented, owing to their advantages. However, these solution strategies have drawbacks, such as the weakness of static implicit in contact configuration for 3D-FE simulation and spring-back estimation for dynamic explicit. Therefore, a coupled method was proposed by Finn et al., 1995 [3] to use the advantages of both approaches.

In sheet metal formation, the forming zone undergoes plastic deformation that weakens the formed section around that area, inducing residual stress/strain. Residual stress stands out as a crucial aspect when dealing with material imperfections. The fatigue durability and strength resistance of a structural element are either positively enhanced or influenced by the existence of residual stress, contingent upon the magnitude and distribution of these stress factors [4,5]. Consequently, process design engineers are keenly interested in obtaining detailed

* Corresponding author.
** Corresponding author.
*** Corresponding author.
E-mail addresses: irwan@uthm.edu.my (J.M. Irwan), aghaleb@alfaisal.edu (A.M. Ghaleb), samiabdo@uthm.edu.my (S. Al-Alimi).

insights into plastic deformation and stress distribution around corners. Various experimental methods have been employed to measure through-thickness residual stresses, such as the sectioning method by Weng and White [5] and layer removal method by Abvabi et al. [6]. Reported results indicate that the through-thickness residual stress distribution takes on a zigzag pattern, with the maximum residual stress occurring either at the bend's inside surface or near the plate's neutral surface. Additionally, several numerical approaches have been undertaken to predict residual stress. Researchers in Refs. [3,6,7] explained the capability of finite element analysis as a time-efficient alternative for predicting residual stresses in thin-walled cold-formed steel sections, especially compared to the time-consuming experimental methods. Quach et al. [4] implemented a 2D finite element technique to predict residual stress, demonstrating good agreement with experimental results in Refs. [7,8].

In numerical analysis, selecting suitable elements is essential based on the outcomes intended to be predicted [1], and it predominantly governs simulation aspects such as contact with friction and CPU time costs [9]. According to Refs. [1,10], the solid element is ideal for such cases to account for plastic deformation in the forming zone. Utilizing solid elements treats the sheet as a 3D entity, providing a more realistic approach to modeling the process. The simultaneous contact on both sides of the sheet is inherently resolved without the need for specific strategies. Additionally, these elements enable precise calculations of stress gradients throughout the sheet's thickness and the evolution of sheet thickness during simulation [11]. Consequently, numerous studies have utilized 3D-Solid FE techniques for the forming process, including Chain-Die forming [12–16]. Roll forming such as [17–28]. Press-braking such as [29–31]. Gerbo et al. [32] also investigated cold-bent thick steel, revealing the limitations of the 2D-FE technique in predicting the through-thickness residual stress distribution along the corner region. The 3D solid FE technique clearly indicated the residual stress distribution, particularly for the variations at the corner edge zone.

Chung et al., 2014 [10] explained the weaknesses of implementing a 3D shell element when a through-thickness investigation is required. Despite the shell element's numerical simplicity and computational time efficiency, achieving an adequate and detailed prediction of plastic deformation in the thickness direction is difficult especially when there is a significant stress gradient in the thickness direction. On the other hand, Research indicates that 3D Shell element is a good choice for simulations in which predictions in through-thickness plastic deformation are not required [1,10]. However, various studies have recommended the adoption of the 3D-Shell FE technique, as this element can predict through-thickness residual stress/strain in roll-forming, as reported in Refs. [24,33–38]. Moreover, it enables accurate prediction of the spring-back phenomenon, as reported in Refs. [39,40].

Zeng et al. [41] enhanced the shell element for the cold roll forming of U-channels. They utilized a quadrangular shell element, specifically S4R in Abaqus, to formulate an optimization method rooted in the Response Surface Method. This method, a regression technique, explores relationships between multiple explanatory variables and one or more response variables. The outcomes were validated through comparison with actual product measurements, demonstrating their acceptability. Vorkov et al., 2014 [40] predicted and analyzed the spring-back in the air-bending forming process of two different high-strength steel. They compared the shell element (S4R) with a solid element (C3D8R) in Abaqus. The results show that both elements can predict rebound.

Wang [42] studied the influence of residual stresses of different cold-formed steel sections called "sigma sections" formed either by press braking or roll forming. This study adopted a quadrangular shell element, element S4R, to achieve its objectives in Abaqus. In addition, the dynamic explicit method was the solution strategy for predicting the residual stress/strain. The results were validated against experimental data for longitudinal strain at the inner and outer surfaces. Trzepiecinski & Lemu [39] investigated the effect of computational parameters on the spring-back prediction of press-braked sections. Eight-node quadratic

doubly curved shell elements (S8R) were adopted with the static implicit method in Abaqus for spring-back prediction of the sheet metal. Yao et al. [33] proposed an FE-based method for estimating residual stresses and equivalent plastic strains from cold-formed steel hollow sections. They first determined the residual stresses and coexistent equal plastic strains due to the coiling-uncoiling and transverse bending operations by an analytical method. They introduced them as the initial conditions in a subsequent static implicit FE simulation of welding and shaping operations. The study adopted a quadrangular shell element, S4R, to achieve its objectives in Abaqus. Yao et al. [43] proposed the same FE-based method in elliptical hollow sections (EHS).

Implementing the shell element in the 3D-FE simulation has the advantage that the simulation can be completed in less time than the solid element, as noted by Chung et al. [10]. Thus, previous studies make it their option to achieve their goals, most related to plastic deformation. However, it is mentioned that the shell elements had drawbacks in the plastic deformation through metal sheet thickness [1,10]. These drawbacks are related to accuracy and detailed information [10,44].

In investigating formed metal inner and outer surfaces or its spring-back phenomena, the shell element could be a suitable choice to fulfill the study aims. Yet, selecting the right solution strategy could improve the study's outcomes, such as accuracy in predicting residual stresses, deformation patterns. A static implicit method is implemented to attain the computation parameters' effect on the spring-back of press-braked steel. The process is suitable for spring-back problems [39]. However, it is recommended in Refs. [1,45] that the solution method proposed by Finn et al. [3] for through-thickness investigation. Therefore, it is suitable to adopt the proposed method to investigate the distribution of residual stresses of steel sheets in the through-thickness direction. Table 1 summarize the studies and elements implemented.

This paper presents an investigation into the utilization of the 3D-Shell FE technique for predicting residual stress distribution in pressed-braked thin-walled steel sections. The primary objective is to offer a comprehensive comparison with the 3D-Solid FE technique, aiming to assess the predictive capabilities of the 3D-Shell FE technique for residual stress analysis. Through this study, we provide a detailed analysis comparing the distribution of longitudinal/transverse residual stresses across the through-thickness of the formed section, compared with findings from the 3D-Solid FE analysis. This comparative analysis highlights the novelty of our research, shedding light on the efficacy and potential advancements of the 3D-Shell FE technique in predicting residual stresses accurately in thin-walled steel sections subjected to pressing and braking operations.

2. Materials and methods

This section describes the procedures to develop the 3D-FE technique for predicting residual stress.

2.1. FE modeling of sheet metal forming & 3D-Shell element formulation

The finite element (FE) analysis was adopted by many engineers for parametric studies, such as modeling the cold roll forming process. Special attention to the FE models (FEM) is needed for the evaluation of the manufacturing parameters to attain high-level quality and cost optimization. Nowadays, implementing finite element analysis in the

Table 1
Summary of the studies and element type implemented.

Forming Method	Finite element	
	Solid Element	Shell Element
Chain Die Forming	[12–16]	–
Roll Forming	[17–28]	[24,33–38,42]
Press-braking	[29–31]	[39,40,42]
Cold bent of thick plate	[32]	–

forming processes involving complex contacts and spring-back problems, such as the simulation of press-braking processes, can be performed with acceptable accuracy. Most recent numerical studies emphasize adopting finite elements, formulations, or integration approaches to assess the deformations in the strip-bent regions (known later as "the corners"). In addition, special attention was given to the stamping processes based on various changes in thickness (or the spring-back) and the accurate definition of the material's mechanical behavior.

The finite element analysis of press-braking contains two stages (Forming and Spring-back). Numerous studies proposed a dynamic explicit approach over an implicit one in the sheet metal forming stage [3,46]. The dynamic clear method operates on an inertia-based process, eliminating the need for static equilibrium. However, this method exhibits conditional stability, requiring the implementation of mass or time scaling procedures. One advantage of the explicit approach is the ability to resolve complicated contact problems. Furthermore, it requires fewer system resources in large models compared to the implicit approach. So far, the implicit approach has merit in handling spring-back calculation more efficiently. Thus, Finn et al., 1995 [3] introduced the coupled method to take advantage of both methods. Their proposed approach used an explicit approach to the model-forming process, while the implicit approach is used for spring-back modeling.

The proposed solution method introduced by Finn et al., 1995 [3] indicates that the forming process will have two stages. The first stage is Forming, which is simulated by the dynamic explicit method. The second stage is Spring-back, which is affected by the static implicit method. For the boundary conditions in the first stage, the die was constrained in all directions with fixed boundary conditions at a predetermined reference point (RP). The loading in the form of displacement control was applied to the punch to allow movement in the y-direction only to form the steel sheet.

3D-Shell element formulation is presented as follow:

The quadrilateral flat shell element, as shown in Fig. 1, The field displacement of this element is approximately determined by Eq. (1). It should be noted that effect of rotation of the flat shell in-plane direction ($\theta_2^{(e)}$) is neglected due to its insignificant impact.

$$
\begin{Bmatrix} u_{ox}^{(e)} \\ u_{oy}^{(e)} \\ u_{oz}^{(e)} \\ \theta_1^{(e)} \\ \theta_2^{(e)} \end{Bmatrix} = \left[\left[N_1^{(4Q)}(\xi,\eta) \right] \left[N_2^{(4Q)}(\xi,\eta) \right] \left[N_3^{(4Q)}(\xi,\eta) \right] \left[N_4^{(4Q)}(\xi,\eta) \right] \right] \begin{Bmatrix} U_1^{(e)} \\ U_2^{(e)} \\ U_3^{(e)} \\ U_4^{(e)} \end{Bmatrix}
$$

(1)

Where $u_{ox}^{(e)}$, $u_{oy}^{(e)}$ and $u_{oz}^{(e)}$ are the element field displacements, $\theta_1^{(e)}$ and $\theta_2^{(e)}$

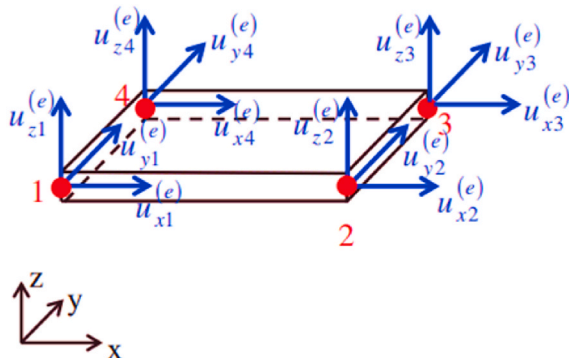rotation in $x-$ and $y-$ direction, $N_1{}^{(4Q)}(\xi,\eta), N_2{}^{(4Q)}(\xi,\eta),$ $N_3{}^{(4Q)}(\xi,\eta)$ and $N_4{}^{(4Q)}(\xi,\eta)$ are the shape function of the element that are determined in the parametric coordinate, $U_1^{(e)}, U_2^{(e)}, U_3^{(e)}$ and $U_4^{(e)}$ are the nodal displacement of the element.

In order to establish relationship between the parametric space and physical space, the following mapping coordinate is needed to need.

$$
x(\xi,\eta) = N_1^{(4Q)}(\xi,\eta)\, x_1^{(e)} + N_2^{(4Q)}(\xi,\eta)\, x_2^{(e)} + N_3^{(4Q)}(\xi,\eta)\, x_3^{(e)} + N_4^{(4Q)}(\xi,\eta)\, x_4^{(e)}
$$
$$
y(\xi,\eta) = N_1^{(4Q)}(\xi,\eta)\, y_1^{(e)} + N_2^{(4Q)}(\xi,\eta)\, y_2^{(e)} + N_3^{(4Q)}(\xi,\eta)\, y_3^{(e)} + N_4^{(4Q)}(\xi,\eta)\, y_4^{(e)}
$$

(2)

Where $x(\xi,\eta)$ and $y(\xi,\eta)$ are the physical coordinates defined in terms of the parametric coordinate, $x_1^{(e)}, x_2^{(e)}, x_3^{(e)}$ and $x_4^{(e)}$ are the coordinate of each node in $x-direction, y_1^{(e)}, y_2^{(e)}, y_3^{(e)}$ and $y_4^{(e)}$ are the coordinate of each node in $y-direction$.

The shape functions in the parametric space with parametric coordinates ξ_g, η_g, where the quadrature point g is given as ($g = 1, 2, ..., N_g$) can be defined as.

$$
N_{1g}^{(4Q)} = N_1^{(4Q)}(\xi_g, \eta_g) = \frac{1}{4}(1 - \xi_g)(1 - \eta_g)
$$
$$
N_{2g}^{(4Q)} = N_2^{(4Q)}(\xi_g, \eta_g) = \frac{1}{4}(1 - \xi_g)(1 - \eta_g)
$$
$$
N_{3g}^{(4Q)} = N_3^{(4Q)}(\xi_g, \eta_g) = \frac{1}{4}(1 - \xi_g)(1 - \eta_g)
$$
$$
N_{4g}^{(4Q)} = N_4^{(4Q)}(\xi_g, \eta_g) = \frac{1}{4}(1 - \xi_g)(1 - \eta_g)
$$

(3)

Then the array of the shape function with size of (5×6) is established to delineate the contribution of node i to the approximate fields.

$$
\left[N_i^{(e)}(\xi,\eta) \right] = \begin{bmatrix} N_i^{(e)}(\xi,\eta) & 0 & 0 & O & 0 & 0 \\ 0 & N_i^{(e)}(\xi,\eta) & 0 & 0 & 0 & 0 \\ 0 & 0 & N_i^{(e)}(\xi,\eta) & 0 & 0 & 0 \\ 0 & 0 & 0 & 0 & -N_i^{(e)}(\xi,\eta) & 0 \\ 0 & 0 & 0 & N_i^{(e)}(\xi,\eta) & 0 & 0 \end{bmatrix}
$$

(4)

The Jacobian matrix [J] of the coordinate mapping is defined as given in Eq. (5).

$$
[J] = \begin{bmatrix} \dfrac{\partial x}{\partial \xi} & \dfrac{\partial y}{\partial \xi} \\ \dfrac{\partial x}{\partial \eta} & \dfrac{\partial y}{\partial \eta} \end{bmatrix} = \begin{bmatrix} \sum\limits_{i=1}^{4}\left(\dfrac{\partial N_i^{(4Q)}}{\partial \xi}\cdot x_i^{(e)} \right) & \sum\limits_{i=1}^{4}\left(\dfrac{\partial N_i^{(4Q)}}{\partial \xi}\cdot y_i^{(e)} \right) \\ \sum\limits_{i=1}^{4}\left(\dfrac{\partial N_i^{(4Q)}}{\partial \eta}\cdot x_i^{(e)} \right) & \sum\limits_{i=1}^{4}\left(\dfrac{\partial N_i^{(4Q)}}{\partial \eta}\cdot y_i^{(e)} \right) \end{bmatrix}
$$
$$
= \left[N_{,\xi}^{(4Q)} \right] \left[\{x^{(e)}\} \{y^{(e)}\} \right]
$$

(5)

Fig. 1. 4-node quadrilateral shell element with nodal degrees of freedom [47].

Where

$$\left[N_{,\xi}^{(4Q)}\right] = \begin{bmatrix} \dfrac{\partial N_1^{(4Q)}}{\partial \xi} & \dfrac{\partial N_2^{(4Q)}}{\partial \xi} & \dfrac{\partial N_3^{(4Q)}}{\partial \xi} & \dfrac{\partial N_4^{(4Q)}}{\partial \xi} \\ \dfrac{\partial N_1^{(4Q)}}{\partial \eta} & \dfrac{\partial N_2^{(4Q)}}{\partial \eta} & \dfrac{\partial N_3^{(4Q)}}{\partial \eta} & \dfrac{\partial N_4^{(4Q)}}{\partial \eta} \end{bmatrix} \tag{6}$$

The derivatives of the shape functions with respect to the physical coordinates, x and y, at $\xi = \xi_g, \eta = \eta_g$, is calculated as expressed by Eq. (7).

$$\left[N_{,x}^{(4Q)}\right]_g = \begin{bmatrix} \dfrac{\partial N_1^{(4Q)}}{\partial x} & \dfrac{\partial N_2^{(4Q)}}{\partial x} & \dfrac{\partial N_3^{(4Q)}}{\partial x} & \dfrac{\partial N_4^{(4Q)}}{\partial x} \\ \dfrac{\partial N_1^{(4Q)}}{\partial y} & \dfrac{\partial N_2^{(4Q)}}{\partial y} & \dfrac{\partial N_3^{(4Q)}}{\partial y} & \dfrac{\partial N_4^{(4Q)}}{\partial y} \end{bmatrix} = \left[\widetilde{J}_g\right]\left[N_{,\xi}^{(4Q)}\right]_g \tag{7}$$

Then the 5×24 array shape function of shell element is defined as given by:

$$\left[N^{(e)}\right]_g = \left[\left[N_1^{(e)}\right]_g \ \left[N_2^{(e)}\right]_g \ \left[N_3^{(e)}\right]_g \ \left[N_4^{(e)}\right]_g \right] \tag{8}$$

Three distinct expressions are written for the membrane $\{\widehat{\varepsilon}_m^{(e)}\}$, bending $\{\widehat{\varepsilon}_f^{(e)}\}$, and shear strains $\{\widehat{\varepsilon}_s^{(e)}\}$ as given below.

$$\left\{\widehat{\varepsilon}_m^{(e)}\right\} = \left[B_m^{(e)}(\xi,\eta)U^{(e)}\right] = \left[\left[B_{m1}^{(e)}(\xi,\eta)\right] \ \left[B_{m2}^{(e)}(\xi,\eta)\right] \ \cdots \ \left[B_{mn}^{(e)}(\xi,\eta)\right] \right] \begin{Bmatrix} \{U_1^{(e)}\} \\ \{U_2^{(e)}\} \\ \vdots \\ \{U_n^{(e)}\} \end{Bmatrix} \tag{9a}$$

$$\left[B_{m_i}^{(e)}[\xi,\eta]\right] = \begin{bmatrix} \dfrac{\partial N_i^{(e)}}{\partial x} & 0 & 0 & 0 & 0 & 0 \\ 0 & \dfrac{\partial N_i^{(e)}}{\partial x} & 0 & 0 & 0 & 0 \\ \dfrac{\partial N_i^{(e)}}{\partial y} & \dfrac{\partial N_i^{(e)}}{\partial y} & 0 & 0 & 0 & 0 \end{bmatrix}, \ \left[B_{f_i}^{(e)}[\xi,\eta]\right] = \begin{bmatrix} 0 & 0 & 0 & 0 & -\dfrac{\partial N_i^{(e)}}{\partial x} & 0 \\ 0 & 0 & 0 & \dfrac{\partial N_i^{(e)}}{\partial y} & 0 & 0 \\ 0 & 0 & 0 & \dfrac{\partial N_i^{(e)}}{\partial x} & -\dfrac{\partial N_i^{(e)}}{\partial y} & 0 \end{bmatrix}$$

$$\left[B_{f_i}^{(e)}[\xi,\eta]\right] = \begin{bmatrix} 0 & 0 & 0 & 0 & -\dfrac{\partial N_i^{(e)}}{\partial x} & 0 \\ 0 & 0 & 0 & \dfrac{\partial N_i^{(e)}}{\partial y} & 0 & 0 \\ 0 & 0 & 0 & \dfrac{\partial N_i^{(e)}}{\partial x} & -\dfrac{\partial N_i^{(e)}}{\partial y} & 0 \end{bmatrix} \tag{10}$$

These strain-displacement arrays are calculated at quadrature point g for each node $[B_{ml}^{(e)}]_g$, $[B_{fl}^{(e)}]_g$, $[B_{sl}^{(e)}]_g$, for each node $I = 1, 2, 3, 4$. Then the 8×24 generalized strain-displacement matrix $[B^{(e)}]$ as well as its transpose are determined. The constitutive stress-strain matrix $[\widehat{D}]$ for the steel material combining material matrix for membrane $[\widehat{D}_m]$, bending $[\widehat{D}_f]$, and shear $[\widehat{D}_s]$ is defined according to Eq. (11) and Eq. (12).

$$[\widehat{D}] = \begin{bmatrix} [\widehat{D}_m] & [0] & [0] \\ [0] & [\widehat{D}_f] & [0] \\ [0] & [0] & [\widehat{D}_s] \end{bmatrix} \tag{11}$$

Where

$$[\widehat{D}_m] = \frac{E.d}{1-v^2}\begin{bmatrix} 1 & v & 0 \\ v & 1 & 0 \\ 0 & 0 & \dfrac{1-v}{2} \end{bmatrix}, \ [\widehat{D}_f] = \frac{E.d^3}{12(1-v^2)}\begin{bmatrix} 1 & v & 0 \\ v & 1 & 0 \\ 0 & 0 & \dfrac{1-v}{2} \end{bmatrix} \ [\widehat{D}_s] = k.G.d\begin{bmatrix} 1 & 0 \\ 0 & 1 \end{bmatrix} \tag{12}$$

$$\left\{\widehat{\varepsilon}_f^{(e)}\right\} = \left[B_f^{(e)}(\xi,\eta)U^{(e)}\right] = \left[\left[B_{f1}^{(e)}(\xi,\eta)\right] \ \left[B_{f2}^{(e)}(\xi,\eta)\right] \ \cdots \ \left[B_{fn}^{(e)}(\xi,\eta)\right] \right] \begin{Bmatrix} \{U_1^{(e)}\} \\ \{U_2^{(e)}\} \\ \vdots \\ \{U_n^{(e)}\} \end{Bmatrix} \tag{9b}$$

The E in Eq. (12) is the steel Young's modulus, d is the shell element thickness, v is the passion ratio, k is the shear correction factor and G is the shear modulus defined as $G = \frac{E}{2(1+v)}$.

Then the distributed forces are calculated $\{p_g\} = \{p(x_g, y_g)\}$. Finally, the flat shell element stiffness $[k^{(e)}]$, and the equivalent nodal force vector, $\{f_\Omega^{(e)}\}$ are calculated according to Eq. (13) and Eq. (14) respectively.

$$\left[k^{(e)}\right] = \iint_{-1-1}^{1\ 1} \left(\left[B^{(e)}\right]^T \left[D^{(e)}\right]\left[B^{(e)}\right] Jd\xi d\eta \right)$$

$$\approx \sum_{g=1}^{Ng} \left(\left[B^{(e)}\right]_g^T \left[D_g\right]\left[B^{(e)}\right]_g J_g W_g \right) \tag{13}$$

$$\left\{\widehat{\varepsilon}_s^{(e)}\right\} = \left[B_s^{(e)}(\xi,\eta)U^{(e)}\right] = \left[\left[B_{s1}^{(e)}(\xi,\eta)\right] \ \left[B_{s2}^{(e)}(\xi,\eta)\right] \ \cdots \ \left[B_{sn}^{(e)}(\xi,\eta)\right] \right] \begin{Bmatrix} \{U_1^{(e)}\} \\ \{U_2^{(e)}\} \\ \vdots \\ \{U_n^{(e)}\} \end{Bmatrix} \tag{9c}$$

$$\left\{f_\Omega^{(e)}\right\} = \iint_{\Omega(e)} \left[N^{(e)}\right]^T \{p\}dV = \iint_{-1-1}^{1\ 1} \left[N^{(e)}(\xi,\eta)\right]^T \{p(\xi,\eta)\}Jd\xi d\eta$$

$$\approx \sum_{g=1}^{Ng} \left(\left[N^{(e)}\right]_g^T \{p_g\} J_g W_g \right) \tag{14}$$

Where $[B_{ml}^{(e)}]$, $[B_{fl}^{(e)}]$ and $[B_{sl}^{(e)}]$ are block strain-displacement arrays for membrane, bending and shear respectively. they can be calculated based on Eq. (10) to Eq. (11) accordingly.

2.2. Model description

This study aimed to form one corner only. Therefore, the dimensions of the sheet were 50 mm wide and 100 mm long to assess the residual

Table 2
Geometrical and Material Properties of a Lipped Channel section.

Specimen	t(mm)	a (mm)	b (mm)	c (mm)	R (mm)	σ_y (MPa)	σ_u (MPa)	ε_y (x 10^{-6})	E (GPa)	n (x10^{-2})	$\varepsilon_u{}^a$%
PBC 14	1.80	76.23	41.45	15.37	3.96	250.1	345.0	1230	203.3	9.56	33
P16	1.63	67.18	34.98	15.82	2.39	220.9	310.7	1090	202.7	9.74	32

stresses that arise from the formed corner of the web flange and the flat region. Thus, the selection of 100 mm length is the highest dimension in the section geometry to be simulated, according to Table 2.

a) Punch and Die dimensions

The essential requirements for die opening and punch size should be counted to form a 90° steel sheet by press braking as given in the following equations [4]:

$$W_d \geq \sqrt{2}(R+t) \tag{15}$$

where W_d, R, and t refer to die opening, intended-formed corner radius, and sheet thickness, respectively. The punch size W_p should be considered as follows:

$$W_p = W_d + 2R(1 - \cos 45^o) \tag{16}$$

As this study is going to establish the 3D-FE approach and compare it with the 2D-FE approach carried out previously by Quach et al. [4], the dimensions adopted for punch and die are similar to the ones described in Ref. [48]. The opening of the die opening was taken as "$W_d = 2.5(R + t)$" shown in Fig. 2.

b) Model and element selection

A rigid analytical model was used to simulate the punch and die, while the steel sheet was modeled as a deformable shell with S4R elements. The S4R element is a 4-node, quadrilateral, stress/displacement shell element with reduced integration and uses a large-strain formulation (ABAQUS 6.13-4). This study was designed to form one corner only. This element was used by Wang [42] to predict the residual stress of cold-formed steel sections. Simpson's rule with 11 integration points was employed for numerical integration across the thickness of the shell wall, where 5–11 integration points are considered adequate, as

suggested by Wagoner & Li, 2007 [49].

c) Material Properties

The nonlinearity of material modeling in (ABAQUS 6.13-4, 2013) [50] is based on the actual stress–plastic strain relationship up to the ultimate point. This stress–plastic strain relationship can be obtained by converting the nominal stress-strain data. The genuine stress-strain relationship and the true stress–logarithmic plastic strain relationship demonstrated in Fig. 2 were established according to equations (3 and 4) and linked to the test done by Weng CC, 1990 [8] on specimens PBC14 and P16. Quach et al., 2006 [4] did not provide an experimental curve of the stress-strain relationship. Furthermore, the geometrical details and material properties of the Cold-form steel section are provided in Table 2.

$$\sigma = E\varepsilon, \varepsilon \leq \sigma_y / E \tag{17}$$

$$\sigma = \sigma_y \left(\frac{E\varepsilon}{\sigma_y}\right)^n, \varepsilon > \sigma_y / E \tag{18}$$

Referring to Table 2 and Fig. 3, σ_y, σ_u ε_y, ε_u and E is the yield strength, the ultimate strength, yield strain, ultimate strain, and Youngs's modulus, respectively. The flange, web, lip, thickness, and corner radius are denoted as b, a, c, t, and R, respectively as illustrated in Fig. 4, and tabulated in Table 2.

d) Assembly and contact definition

The parts of the model were assembled in each stage and the surface-to-surface constrains were utilized to place the model in the exact position. The general contact condition was used to simulate the interaction behavior between parts of the model.
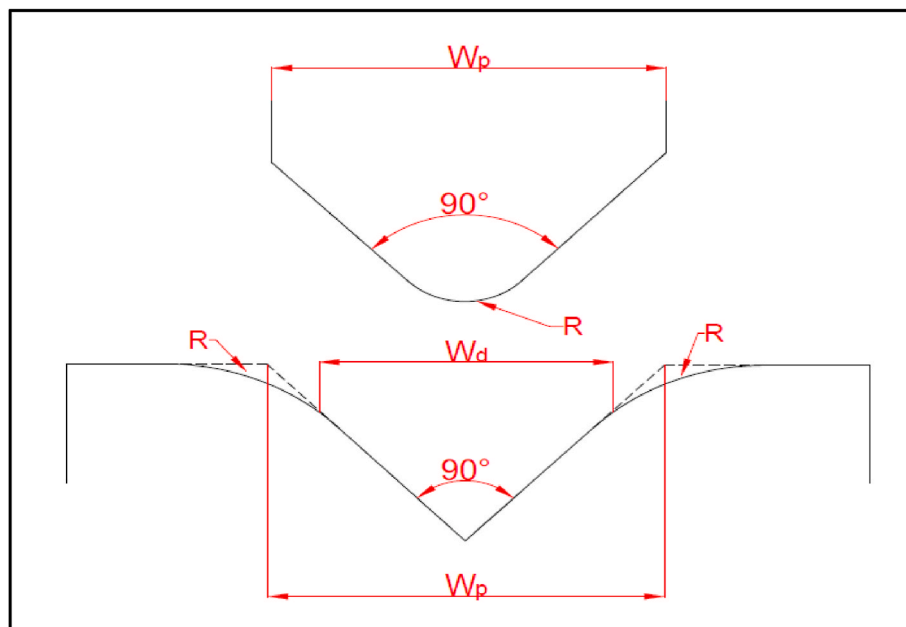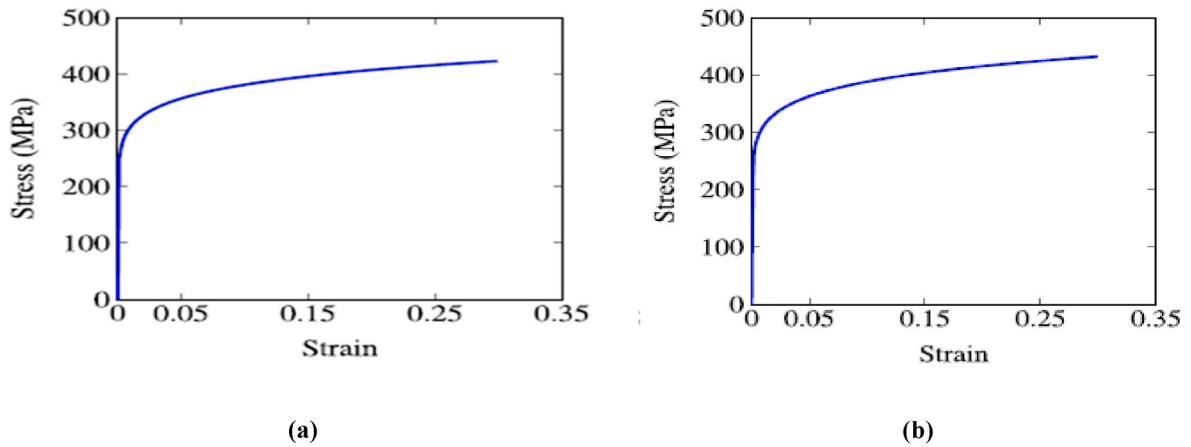

Fig. 2. Die and punch dimensions.

Fig. 3. Stress-strain curve: (a) steel sleeve channel PBC14 and (b) P16 steel lipped channel [51],
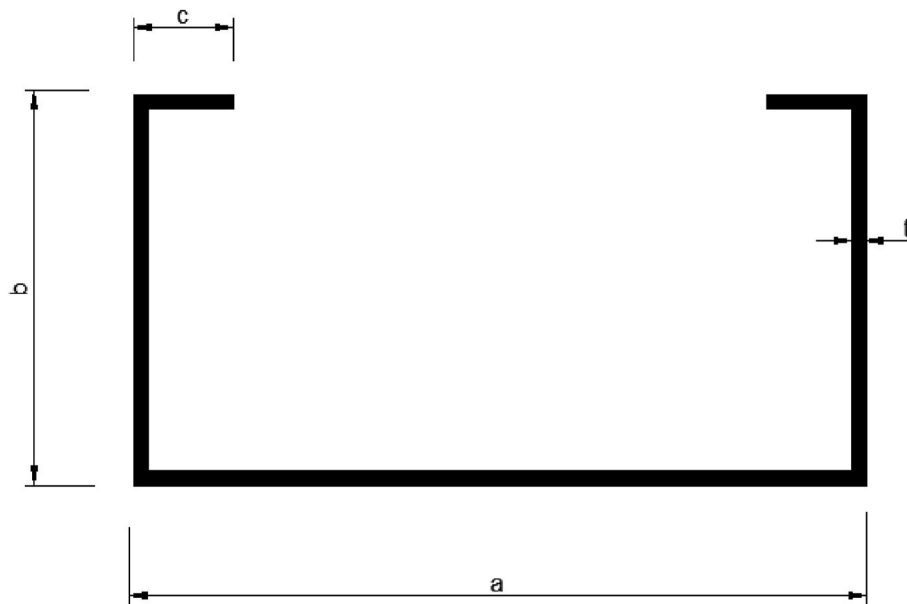

Fig. 4. Dimensions of the lipped channel section.

e) Step definition and Boundary conditions
- Forming (Explicit)

Determining the appropriate time step for the forming process is vital to obtain an acceptable level of accuracy of the results. Generally, the punch speed is recommended to be less than 1 % of steel wave speed (5000 m/s) [50]. Moreover, punch speed for typical forming processes is suggested to be taken as 1 m/s or higher. However, the distance the punch moved in both stages was 0.07 m. Thus, 0.07 m/s was equivalent to the suggested speed, which led to the estimate of the step time to be 0.07s. With several trials, the optimal step time was selected to be 0.1 as the first step exhibited localized damage and kinetic energy more significant than 10 % of internal energy when accompanied with mass scaling (350) to speed up the analysis [50,52].

The die was constrained in all translations and rotations for boundary conditions by implementing fixed boundary conditions to the respective reference point (RP). The load was then applied to the punch using a displacement method in the y-direction only to form the steel sheet.

- Spring-back

For spring-back analysis in both loading stages, it is imperative to omit contacts, rigid parts, and explicit steps, keeping only the deformable part (steel sheet). Before creating the implicit step, the result output of the forming step (Explicit) was considered initial conditions by employing a predefined field (Initial state). Then, create Stage the
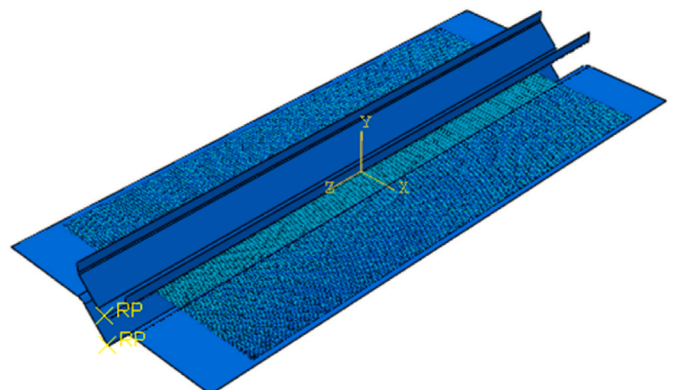

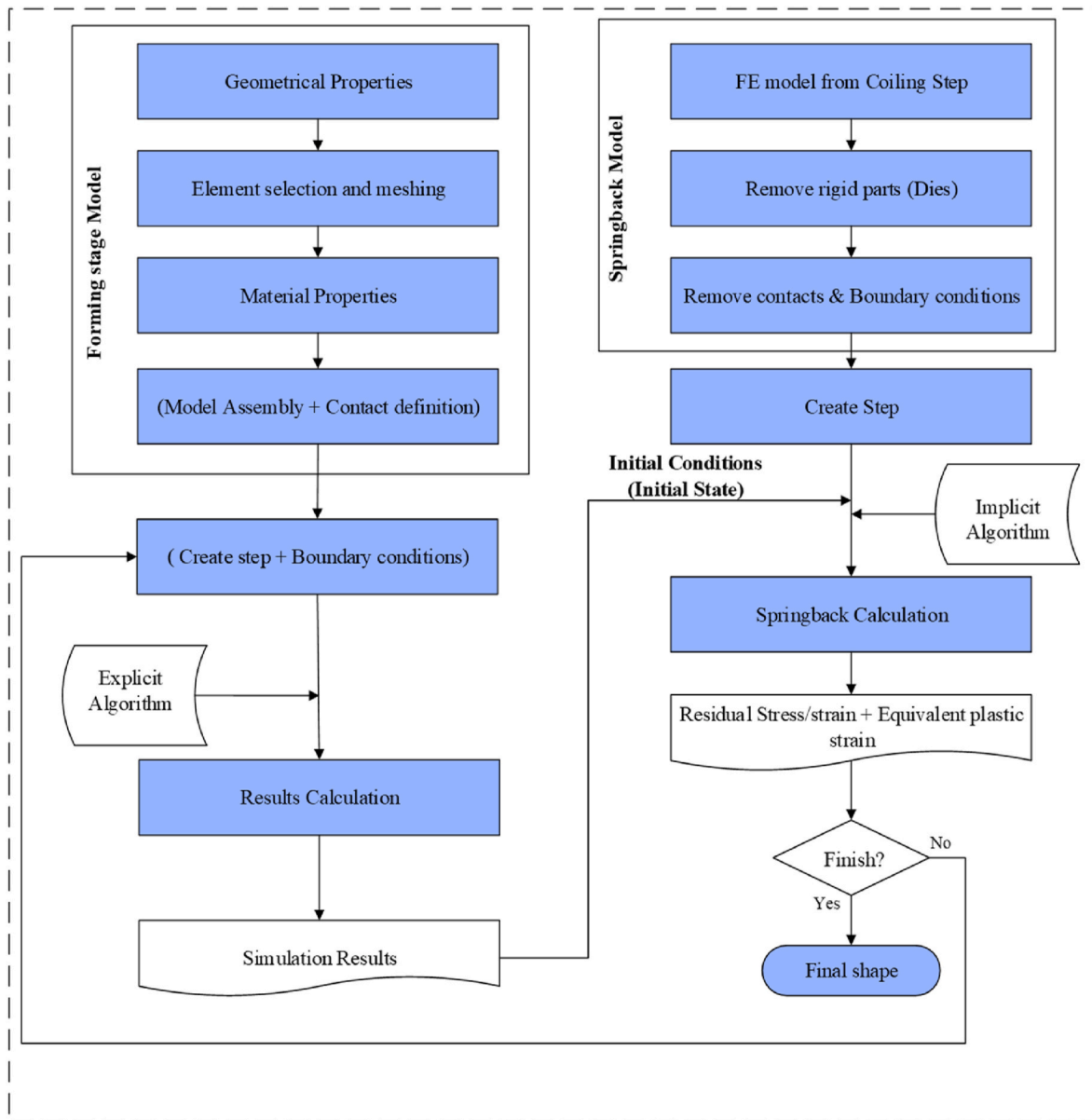**Fig. 5.** FE Modelling configuration.

Fig. 6. Simulation flow chart.

implicit step (General static). The steel sheet was free of restrictions. The configuration of the FE modeling and simulation process is shown in Figs. 5 and 6.

2.3. Mesh convergence study

Mesh sensitivity studies have been performed for a rectangular metal sheet under the metal forming process through a press-braking method to obtain the optimal element distributions in the model. Four different mesh densities were analyzed, and the corresponding residual stresses of the models were compared and evaluated. A finer mesh was provided along with the plate's shorter edge where the interaction of the plate, the punch, and the die occurs; hence, it experienced large bending deformation.

In this study, the distribution of stress along three longitudinal node lines was evaluated. Those lines are the mid-corner line A-A, end-corner line C–C and a line between B–B. See Fig. 7. The steel sheet is divided into three central regions, i.e., a corner region and two flat regions. Points A and C are located at the middle and end of the bend curve,

respectively. Point C is the connection point with the flat line region. The location of the middle and end of the bend curve was selected to validate the findings of the finite element with those of ref. [4,8]. In the convergence study, the maximum tensile and compressive residual stresses were considered as they directly impact the section buckling strength [53]. This study assessed stresses at the longitudinal node line of the mid-corner line (A-A) only. Tables 2 and 3 summarise the findings of the convergence test.

The 50 × 100mm plate is discretized into finite elements in the width and length directions. Four different mesh sizes are presented in this section, indicated by the number of seeds in the width direction and length direction (No. of seeds in width x No. of seeds in length direction). In each mesh size, the number of seeds in the width direction is higher than in the length direction to refine the forming zone. The mesh size of (300 × 150) was selected as a reference to measure the accuracy of the three remaining meshes. It was noticed that the obtained result based on the mesh size of (200 × 150) was in good agreement with the reference mesh, as summarized in Table 3. Therefore, a mesh size of (200 × 150) is adopted for this study. Similarly, the mesh size of (300 × 150) was used
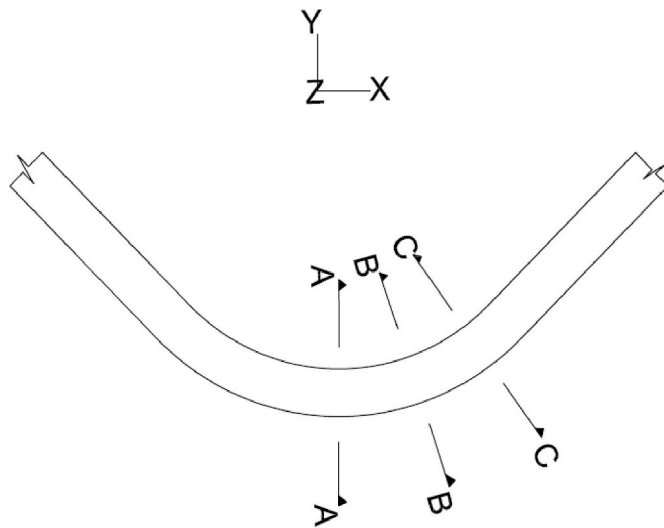
Fig. 7. The selected longitudinal lines.

to measure the accuracy of the other three meshes. The obtained result based on the mesh size of (200 × 150) showed a good agreement with the reference mesh as summarized in Table 4 Therefore, the mesh size of (200 × 150) is adopted for this study.

3. Results and discussion

This section presents results obtained from the 3D-Shell FE technique. First, it begins with results validation and then explains the residual stress distribution. Finally, a comparison of through-thickness variation with the 3D-Solid FE technique.

3.1. Validation of the results

It is important to compare the findings of the FE analyses with independently published research work to validate the performed numerical simulations. Attention was given to the work of Weng CC, 1990 [8] and the results obtained for the 3D-FE technique based on implementing a solid element for validation and comparison purposes.

At flat regions, the residual strain was calculated using a closed-formed analytical solution in Ref. [48] to estimate the residual stresses and the equivalent plastic strains from the coiling-flattening process.

The material's behavior is assumed to be elastic-perfectly plastic, and the transverse to longitudinal stress ratio is expressed as a function of the distance from the mid-plane.

Figs. 8 and 9 demonstrate a good match between this study and previous experimental results [8] and 3D-Solid FE. Therefore, the 3D-Shell FE results of this study are validated. However, there are no differences between the two techniques. However, the results for the outer surface are much closer to the experiment results. The contact between punch and steel sheet can explain the spikes for the inner results.

3.2. Residual stresses distribution

This section discusses residual stress distribution in the corner and flat regions. This section discussed the residual stresses generated due to the press-braking process. The distribution of transverse and longitudinal residual stresses and their maximum tensile and compressive zones were considered.

3.2.1. Longitudinal residual stresses

3.2.1.1. Corner region. The distribution of residual stresses in the longitudinal direction reveals that compressive stresses occur at the corner region's inner surface. In contrast, tensile stresses occur at the same region's outer surface, as shown in Figs. 10 and 11. These residual stresses reach their highest values in the area close to the middle surface. Fig. 10a and 11a show that most inner corner regions experienced compressive residual stresses. It recorded its ultimate values close to the edge, relatively away from the mid-corner line. Furthermore, the small skirted zones at the mid-corner edges experienced some residual tensile stresses. As shown in Fig. 10k 11k, the residual tensile stresses were observed to take place in nearly the entire outer corner area. Their ultimate values were near the edge from the mid-corner line, with compressive stresses in the small skirted area at the mid-corner edges.

The middle surface has the highest longitudinal tensile and compressive residual stresses. Fig. 10e and 11e depict longitudinal compressive stresses at the upper layer of the middle layer approaching the inner surface. In this layer, residual stresses approach their highest. The stress distribution reveals that compressive residual stresses recorded their ultimate values away from the mid-corner, then they gradually reduce toward both the corner end and edge. The longitudinal tensile residual stresses at a layer below the middle layer toward the outer surface are shown in Fig. 10g and 11g. Tensile residual stresses in this layer are the highest and propagate longitudinally from the midpoint of
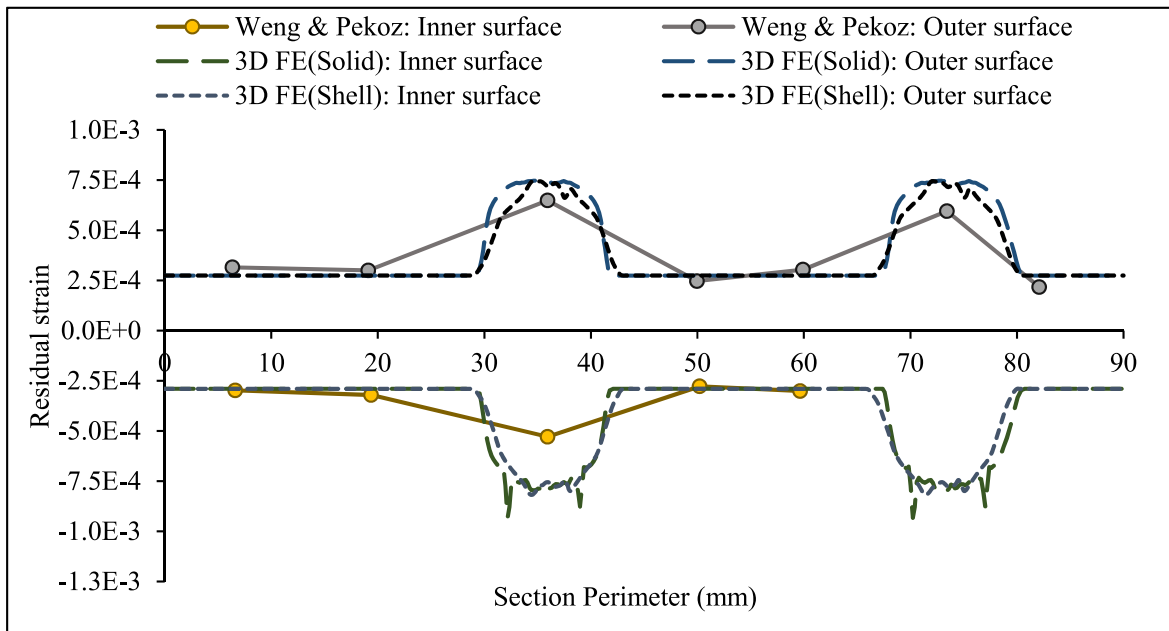
Table 3
Comparison of the maximum tensile and compressive stresses for specimen PBC14 at the mid-corner line (A-A).

Mesh	No. of elements	Max. compressive residual stresses				Max. tensile residual stresses			
		$\sigma_{Tran.}$ (MPa)	Diff. %	$\sigma_{Long.}$ (MPa)	Diff.%	$\sigma_{Tran.}$ (MPa)	Diff. %	$\sigma_{Long.}$ (MPa)	Diff.%
150 × 100	15000	278.74	0.75	164.58	0.22	−330.76	1.86	−164.91	−2.13
200 × 100	20000	275.95	−0.26	164.35	0.08	−320.08	−1.43	−166.00	−1.48
200 × 150 **Adopted**	30000	276.83	0.06	162.66	−0.95	−321.03	−1.13	−170.13	0.97
300 × 150	45000	276.66	–	164.22	–	−324.71	–	−168.50	–

Table 4
Comparison of the maximum tensile and compressive stresses for specimen P16 at the mid-corner line (A-A).

Mesh	No. of elements	Max. tensile residual stresses				Max. compressive residual stresses			
		$\sigma_{Tran.}$ (MPa)	Diff. %	$\sigma_{Long.}$ (MPa)	Diff.%	$\sigma_{Tran.}$ (MPa)	Diff. %	$\sigma_{Long.}$ (MPa)	Diff %
150 × 100	15000	−285.64	3.12	−156.71	2.36	265.13	2.52	158.39	0.13
200 × 100	20000	−270.00	8.43	−150.48	1.71	260.83	0.86	158.42	0.15
200 × 150 **Adopted**	30000	−288.65	2.1	−150.71	1.56	233.42	9.74	156.56	1.02
300 × 150	45000	−294.85	–	−153.10	–	258.61	–	158.18	–

Fig. 8. Comparison of the residual strain of section PBC14.
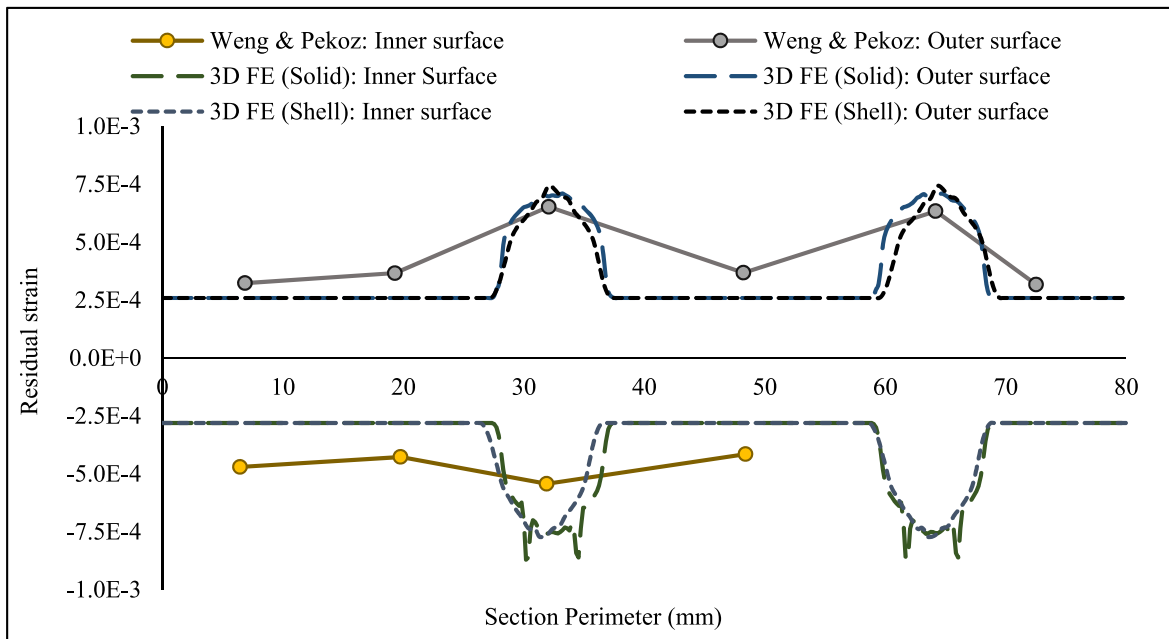

Fig. 9. Comparison of the residual strain of section P16.

the corner line to the corner ends. As a result, they decrease near the end and edge of the corner. Even though tensile residual stresses predominate in the middle layer, both tensile and compressive residual stresses exist. The corner edge experiences compressive residual stresses that sharply decrease and become dominant by tensile residual stresses, as shown in Fig. 10f and 11f.

3.2.1.2. Flat region. The residual stresses from the coiling and uncoiling processes are negligible in this region because the coil diameter is D = 1100 mm. Figs. 10 and 11 show how sensitive the forming process is to the coiling diameter, showing the presence of residual stresses in the flat region due to this operation. However, these stresses do not follow the distribution of the corner region. Instead, the plate's top surface exhibits

tensile residual stress, while the plate's bottom surface exhibits compressive residual stress. Furthermore, residual stresses are highest in the top and bottom layers. They reached their maximum values near the edge's corner region. This phenomenon is known as the "edge effect," it is predicted that stresses will be generated when a plate comes into contact with a die.

3.2.2. Transverse residual stresses

3.2.2.1. Corner region. A wide range of the inner surface at the corner zone experiences tensile residual stresses. These stresses were recorded at values higher near the corner edge than the corner region. On the other hand, they progressively decrease after the mid-corner line to the
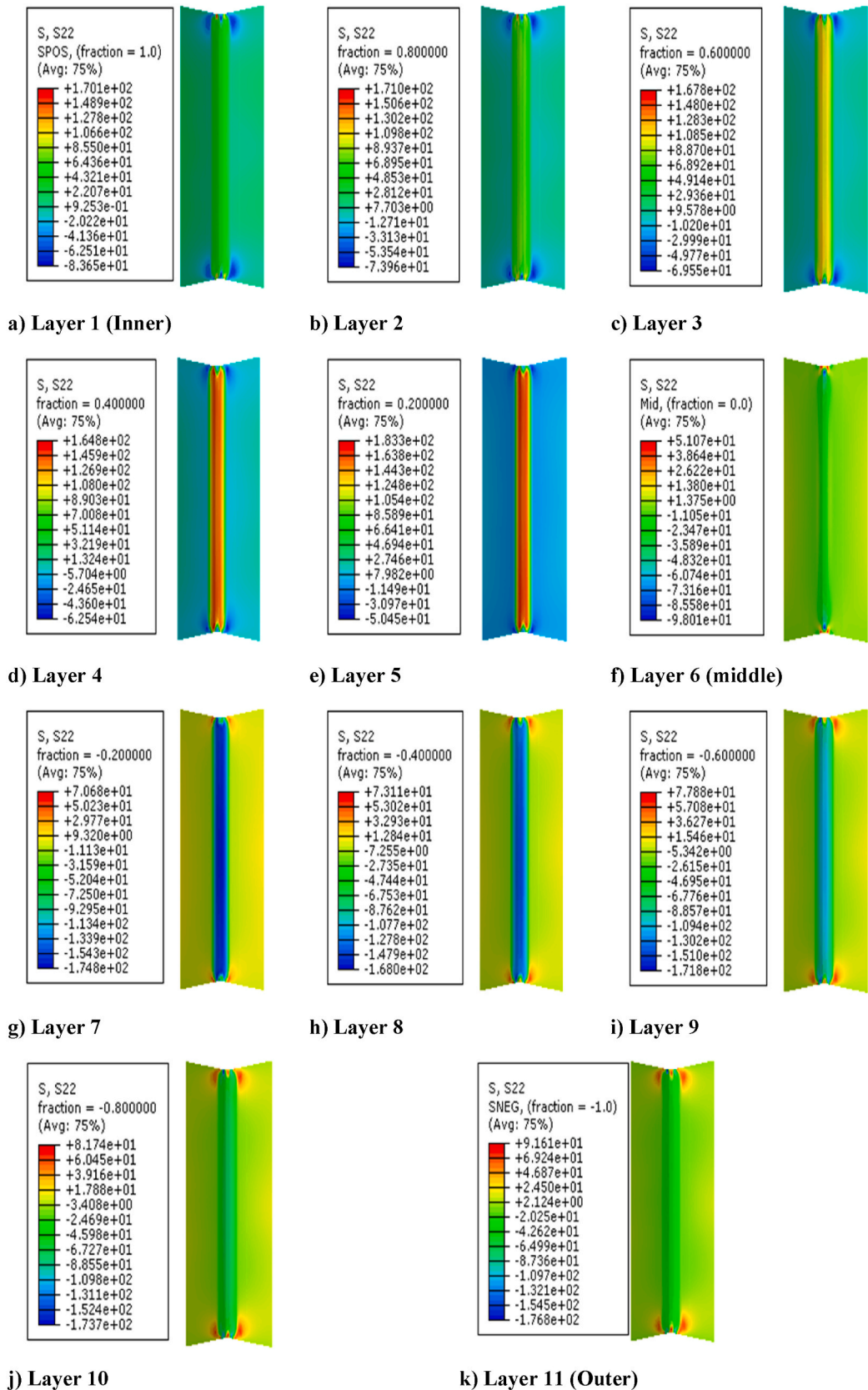
a) Layer 1 (Inner) **b) Layer 2** **c) Layer 3**

d) Layer 4 **e) Layer 5** **f) Layer 6 (middle)**

g) Layer 7 **h) Layer 8** **i) Layer 9**

j) Layer 10 **k) Layer 11 (Outer)**

Fig. 10. Distribution of longitudinal residual stresses in the corners and flat regions of PBC14 specimen.

a) Layer 1 (Inner)

b) Layer 2

c) Layer 3

d) Layer 4

e) Layer 5

f) Layer 6 (middle)

g) Layer 7

h) Layer 8

Layer 9

i)

j) Layer 10

k) Layer 11 (Outer)
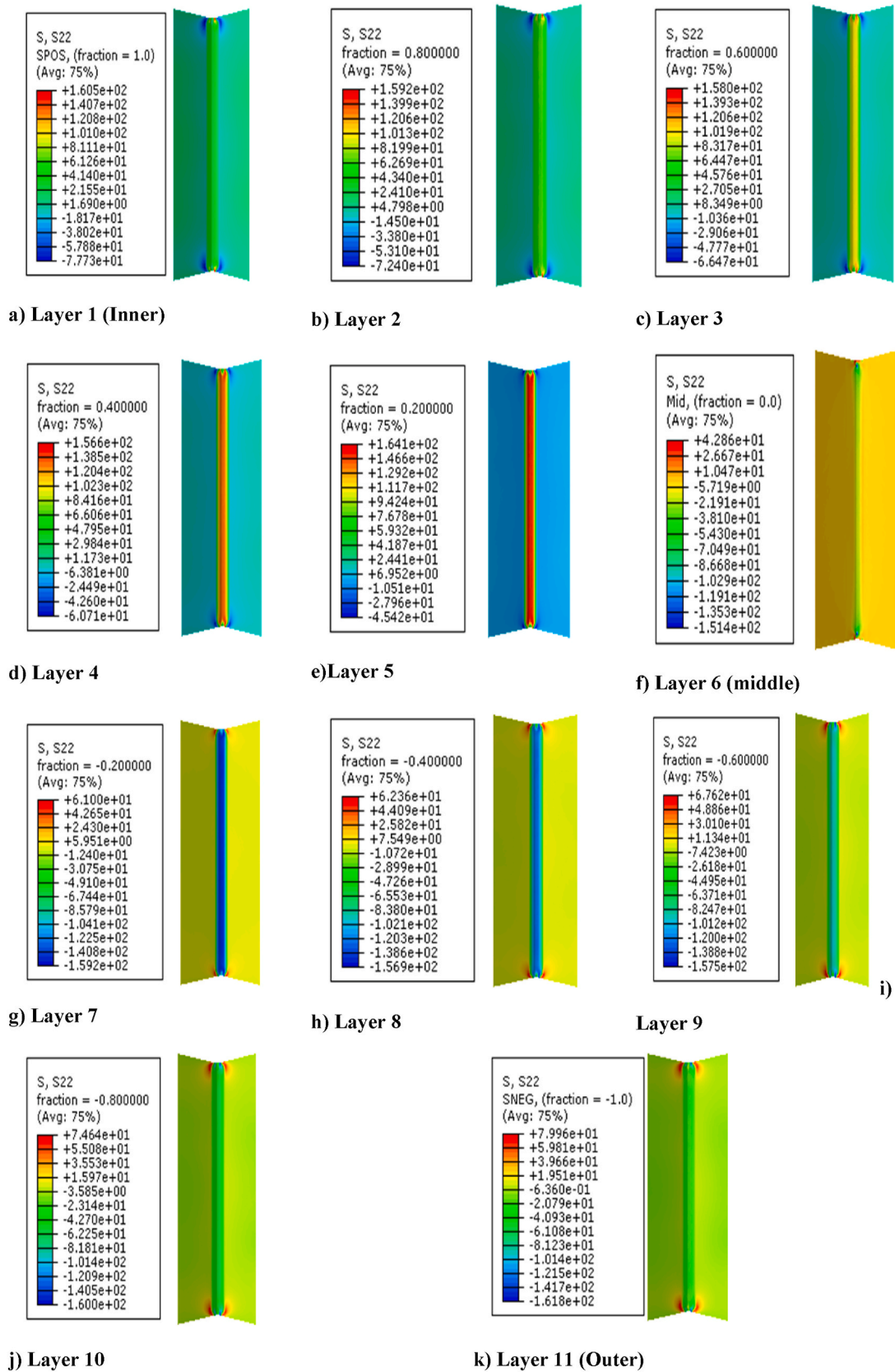
Fig. 11. Distribution of longitudinal residual stresses in the corners and flat regions of P16 specimen.
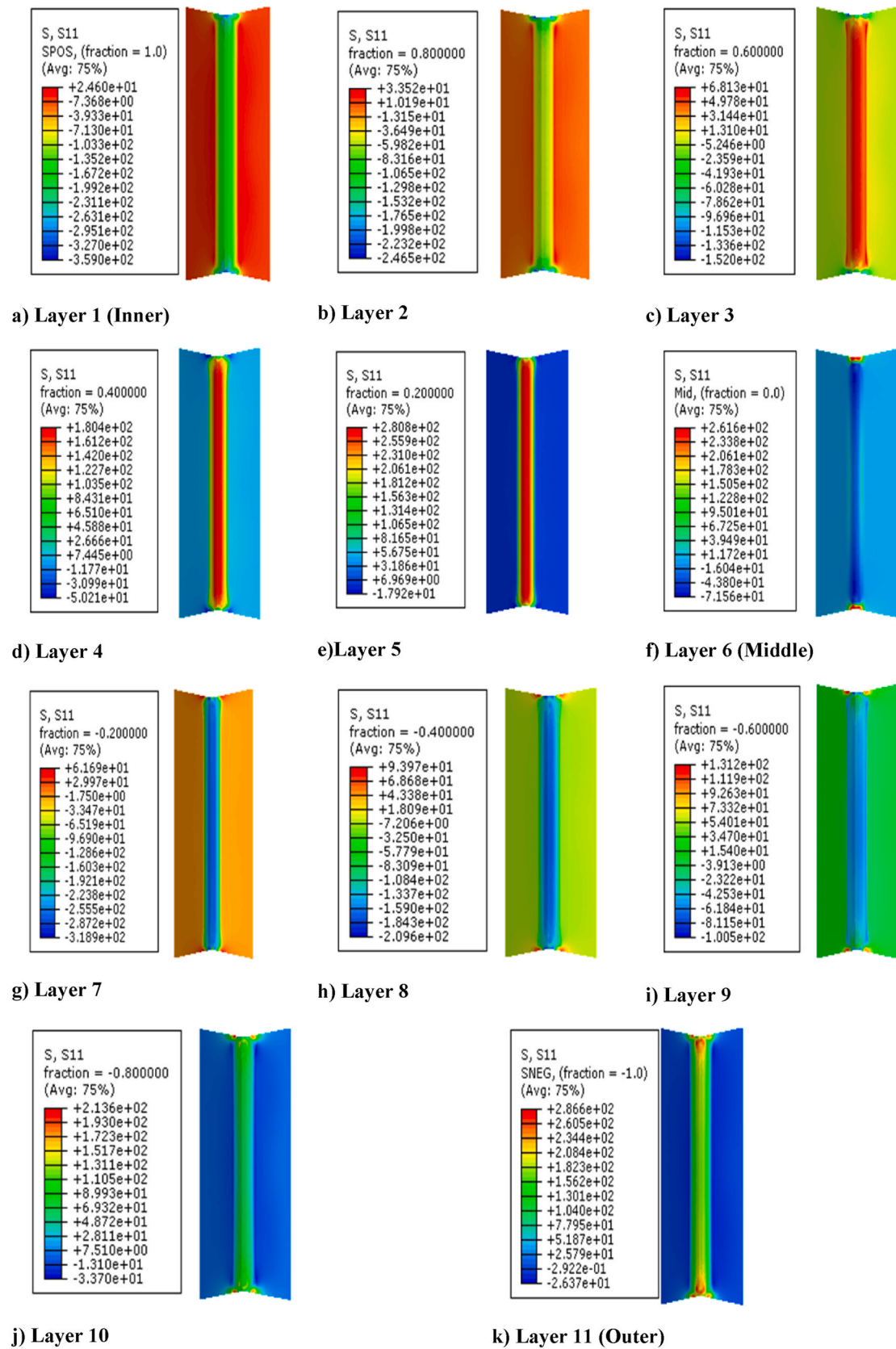
Fig. 12. Distribution of transverse residual stresses in corner and flat regions PBC14 sample.
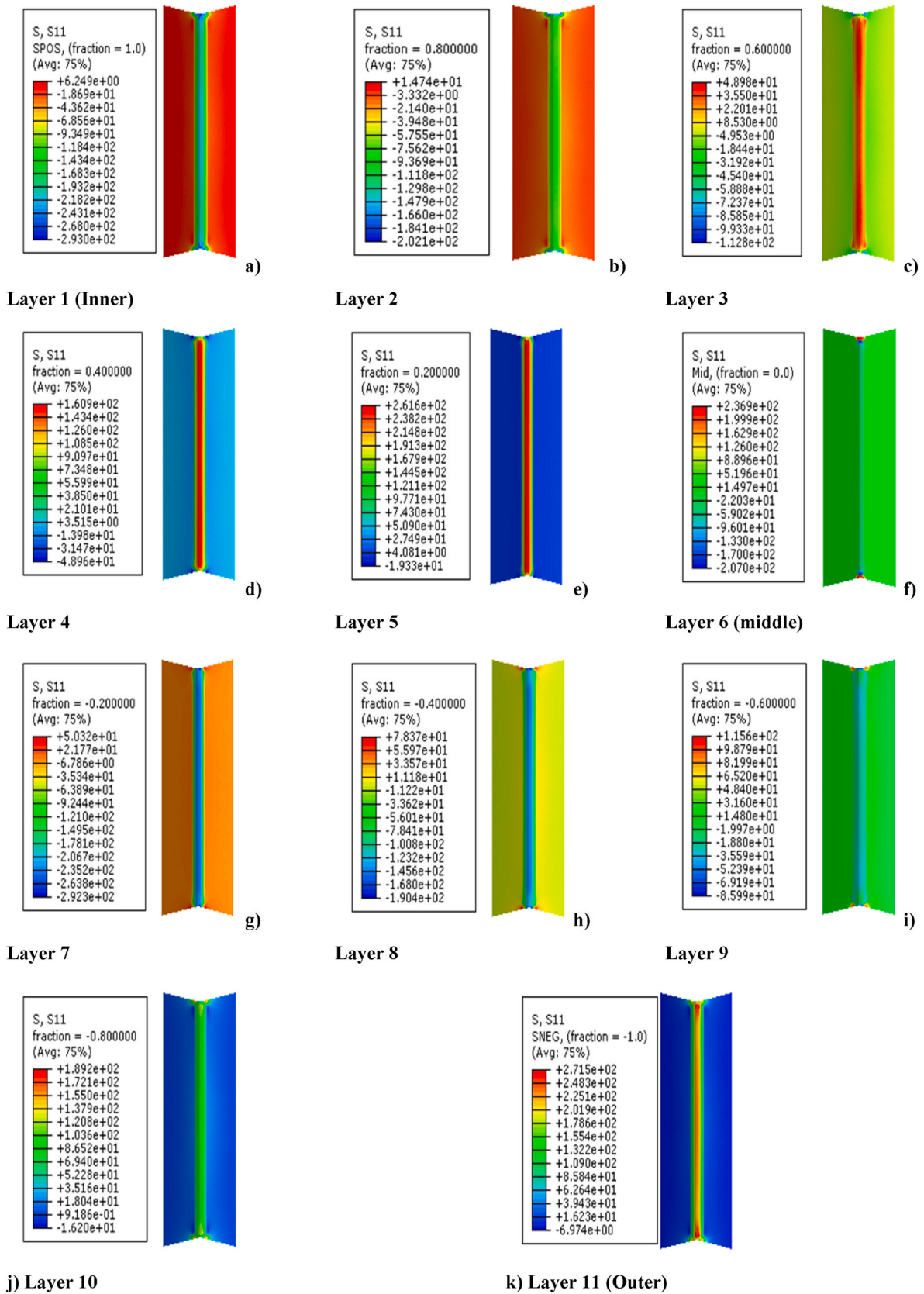
Fig. 13. Transverse residual stresses distribution at the corner and flat regions P16 specimen.

corner ends, as shown in Fig. 12a and 13a. The high intensity of the compressive residual stresses is observed at the mid-corner line of the outer surface, which decreases as the corner ends (Fig. 12k and 13k).

The ultimate transverse residual stresses exist within layers above and below the middle layer. Compressive residual stresses occur in the mid-layer upper layer toward the inner surface. Fig. 12e and 13e show the contours of the compressive residual stresses along the corner region. Fig. 12g and 13g show the tensile residual stresses beneath the middle layer toward the outer surface. These residual stresses intensified near the mid-corner line, slightly dropping toward the corner end. Tensile residual stresses are present in the mid-layer, as shown in Fig. 11f and 12f, resulting from a mix of compressive and tensile transverse residual stresses, where compressive residual stresses and the mid-corner zone occupy edges.

3.2.2.2. Flat region. Figs. 12 and 13 show an evolution of residual stresses generated from the press-braking process. The stress distribution of this region is similar to the corner, where the tensile residual stresses and compressive stresses are in the top and bottom layers, respectively.

3.3. Through-thickness variation and comparison with the 3D-FE solid technique

This part elaborates on the residual stresses throughout the corner area based on the variation in thickness. It also compares these findings to the results reported in Refs. [4,8].

3.3.1. Maximum residual stresses comparison

Based on results reported in Ref. [8], longitudinal residual stresses at the corner region are between 0.25 and 0.7 σ_y yield stress. Additionally, residual tensile stresses were observed at the outer surface, whereas residual compression stresses were found on the inner surface. On the other hand, according to the 2D finite element analysis results reported in Ref. [4], the ultimate longitudinal and transverse compression residual stresses at mid-corner (A-A) were 0.9 σ_y and 1.4 σ_y, respectively, In contrast, the maximum longitudinal and transverse tensile residual stresses at mid-surface were 0.5 σ_y and 0.8 σ_y, respectively. Furthermore, near the corner end, the ultimate tensile residual stresses at the transverse direction (C–C) were approximately 0.9 σ_y and 1.1 σ_y for compressive once and identified in the middle of the plate's surface.

This study used the method described [4] to compare the results. Thus, the results for mid-corner lines (A-A), (B–B), and near-end-corner (C–C) were given in this section. The residual stress distributions in both directions for A-A and C–C are shown in Figs. 14–17. As stated earlier, Simpson's rule with 11 integrated points was assigned to the plate model hence the plate thickness was divided into 11 layers. The maximum longitudinal compressive and tensile residual stresses were approximately 0.68 σ_y and 0.65 σ_y at the mid-corner zone, respectively (Fig. 13), and they are located near the middle layer of the plate. Furthermore, the ultimate transverse compressive and tensile residual stresses near the mid-layer are 1.28 σ_y and 1.11 σ_y, respectively, as shown in Fig. 15. In contrast, the longitudinal compressive and longitudinal tensile residual stresses were found to be 0.5 σ_y and 0.52 σ_y near the mid-layer of the corner end, respectively, as shown in Fig. 16. According to Fig. 17, the transverse residual stresses near the corner end revealed that the maximum magnitude of compressive stress is almost 1.14 σ_y near the mid-layer. The maximum tensile residual stress is about 0.85 σ_y near the mid-layer. As a result, there is a strong correlation between the findings of this study and the findings of [4,8]. The summary of the comparison between the current work and ref. [4,8], including findings for the 3D-Solid FE technique, are shown in Table 5.

The residual stresses in the longitudinal and transverse directions decreased from the middle to the end of the corner zone. Nonetheless, the tensile residual stresses in the transverse direction are greater at sections C-C than at sections B-B. This could be because the punch part interacts with the plate near the plate edge during the loading process. Furthermore, Table 5 shows that the 3D-Shell FE has higher ultimate tensile stresses than the 3D-Solid FE and 2D-FE but lower compressive stresses.
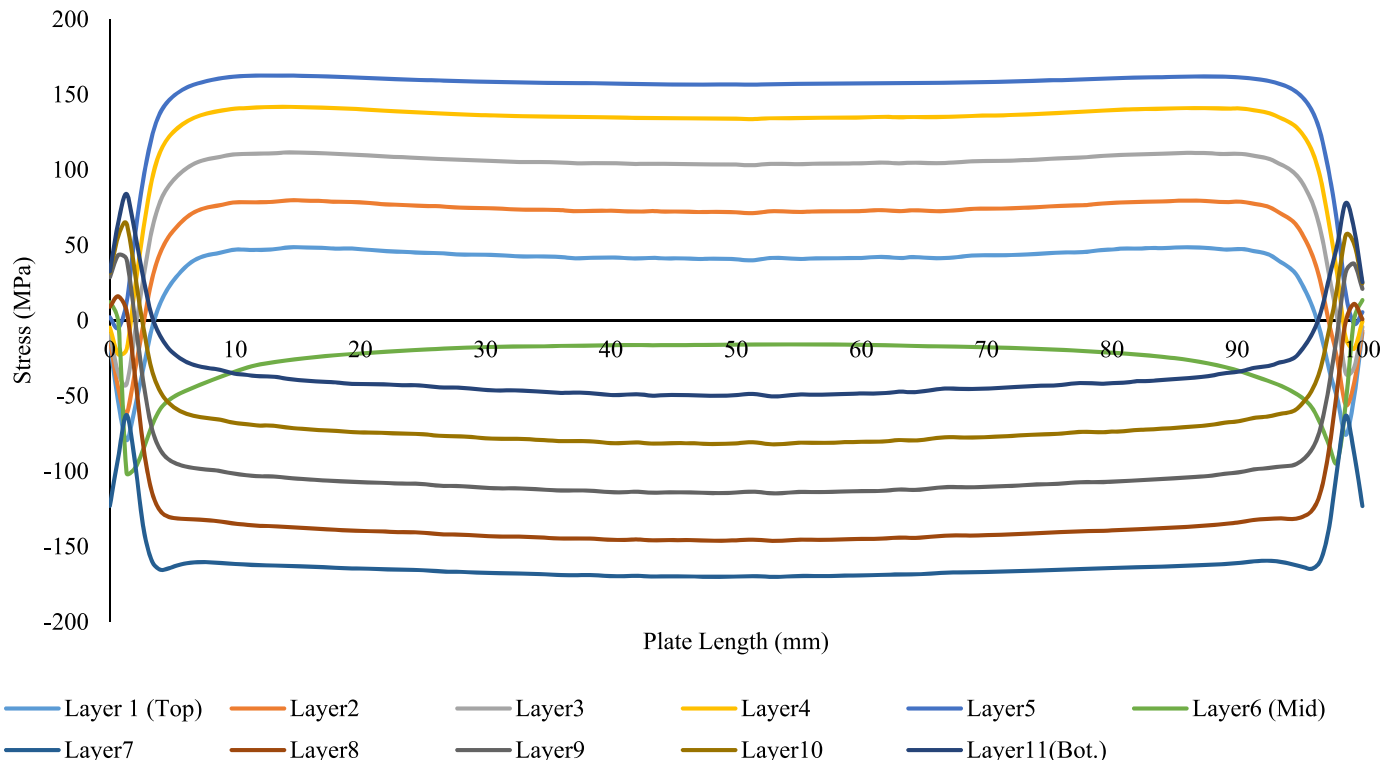

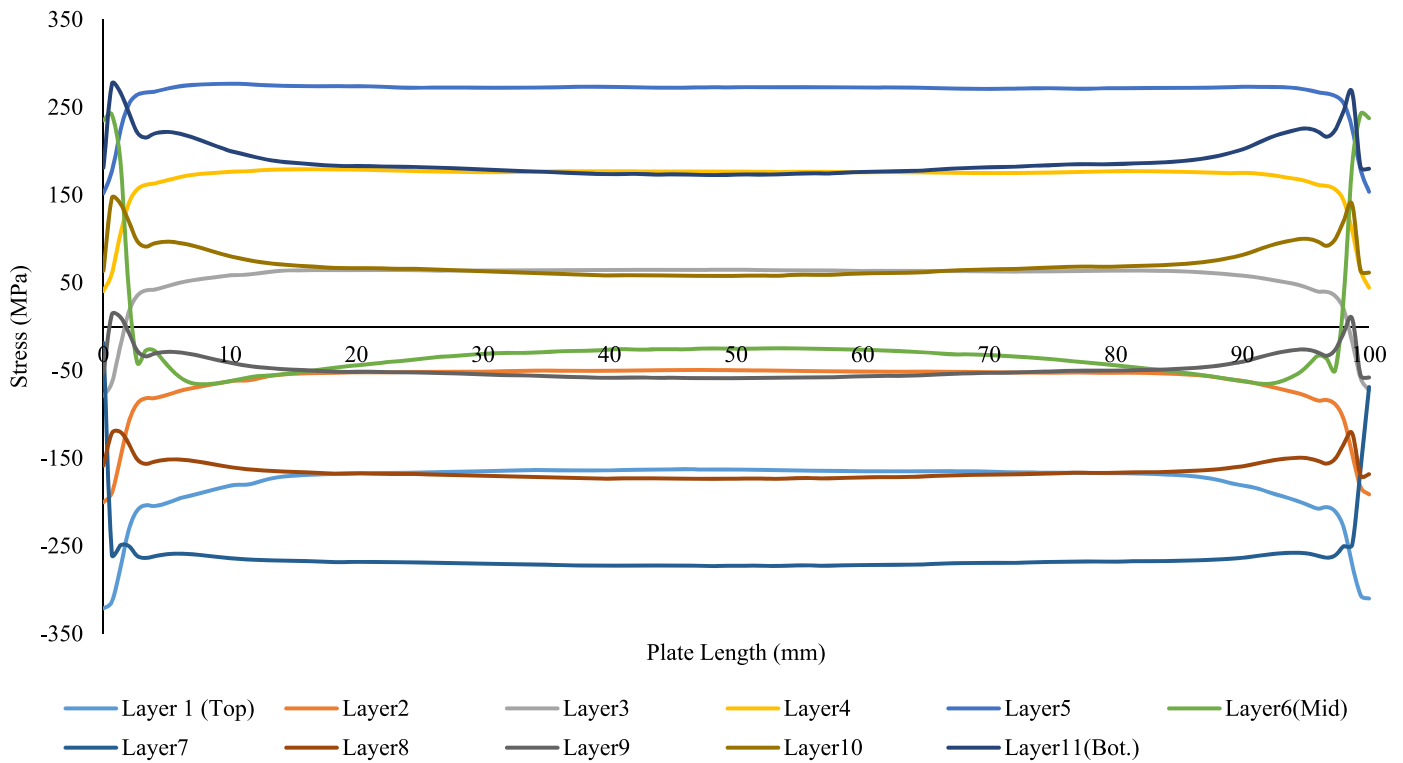**Fig. 14.** Longitudinal residual stresses of PBC14 in A-A.

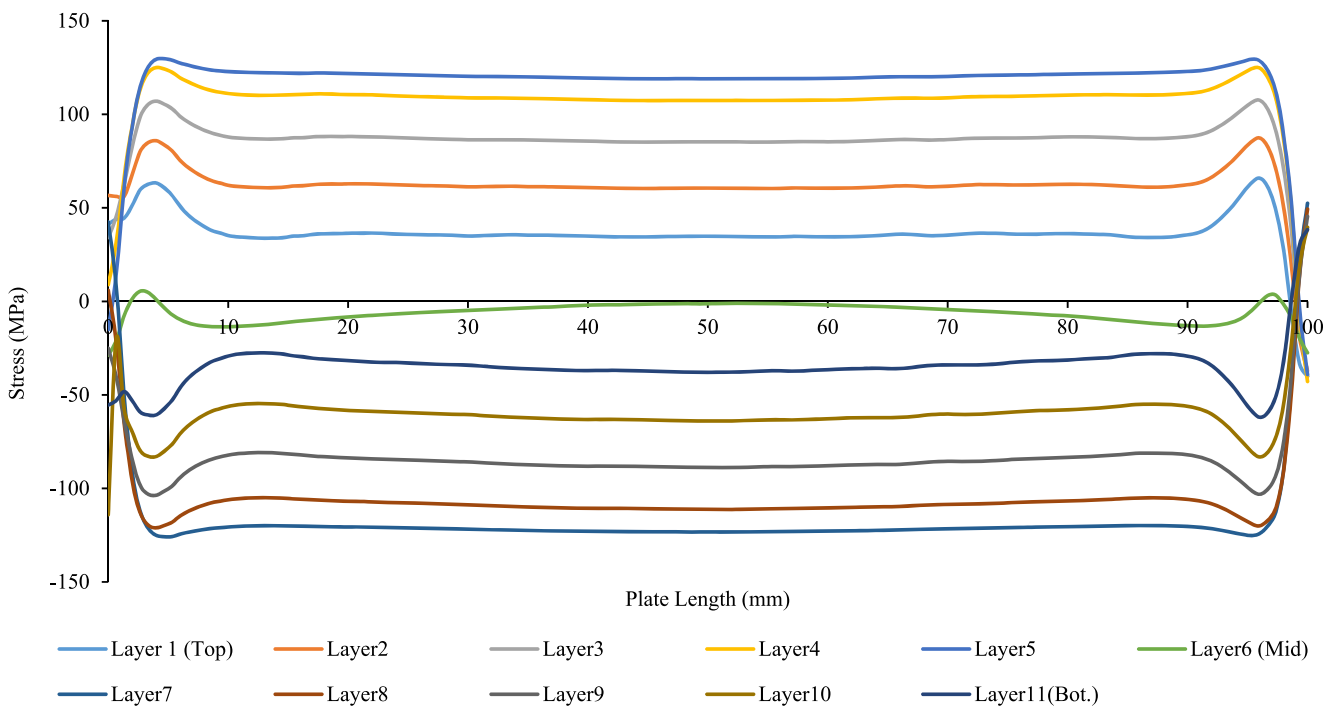**Fig. 15.** Transverse residual stresses of PBC14 at A-A.

Fig. 16. Longitudinal residual stresses of PBC14 in CC.

3.4. Through-thickness residual stresses variation

This section compares the residual stress through-thickness variation obtained from the 3D-Shell FE technique to those obtained from the 3D-Solid FE technique.

3.4.1. Longitudinal through-thickness residual stress variation

Fig. 18 illustrates the distribution of longitudinal stress at mid-corner (A-A). The distribution form shows that solid and shell elements have similarities at x = 4 mm, 20 mm, 50 mm. however, at x = 0.7 mm they differ in distribution form. At x = 0.7 mm, both elements show tensile
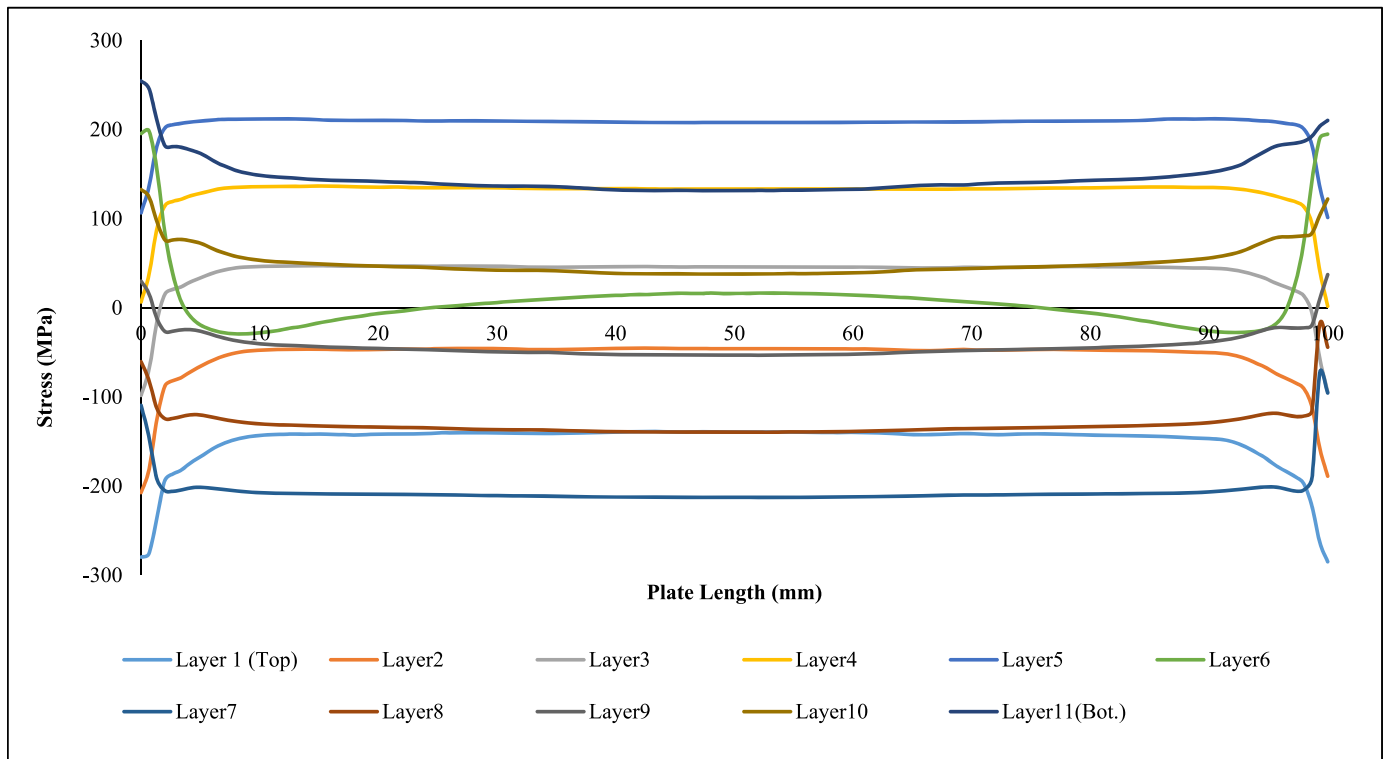
Fig. 17. Transverse residual stresses of PBC14 at C–C.

Table 5
Comparison of Tensile and compressive residual stresses.

Reference	A-A (Mid-corner)				B–B				C–C (Near-end corner)			
	σ_z/σ_y		σ_x/σ_y		σ_z/σ_y		σ_x/σ_y		σ_z/σ_y		σ_x/σ_y	
	Tensile	Comp.	Tensile	Comp.	Tensile	Comp.	Tensile	Comp.	Tensile	Comp.	Tensile	Comp.
Experiment (Weng CC, 1990)	0.25 - 0.7		–	–	0.25 - 0.7		–	–	0.25 - 0.7		–	–
2D-FE (Quach et al., 2006)	0.5	0.9	0.8	1.4	0.43	0.78	0.86	1.1	0.46	0.73	0.9	1.1
3D-Solid FE (PBC14 Specimen) (Mutafi et al., 2019)	0.42	0.87	0.77	1.25	0.43	0.81	0.83	1.13	0.45	0.61	1.01	1.02
3D-Shell FE (PBC14 Specimen)	0.68	0.65	1.28	1.11	0.63	0.64	1.07	1.07	0.5	0.52	1.14	0.85

residual stress at the inner surface and compressive residual stress at the outer surface. Shell element is significantly higher than the solid element at the inner surface. Approach its peak compressive residual stress on the outer surface, where the solid element exists below the mid-surface. At x = 4 mm, the shell and the solid elements differ on surfaces where the shell shows a compressive residual stress on the inner and tensile residual stress on the outer surface. Both elements reach their peak compressive residual stress above the midsurface, although the solid element is higher than the shell element. For tensile residual stress, solid elements approach it slightly above the mid-surface, whereas shell elements approach it below the mid-surface. For longitudinal residual stress distribution at x = 20 mm, 50 mm, similar distribution form for both elements. The inner surface contains compression stresses and the outer is tensile. Similarly to x = 4 mm, the maximum compressive residual stress exists above the mid-surface for both elements. ultimate tensile residual stress exists below the mid-surface for the shell elements and at the mid-surface for the solid elements. In general, shell peak compressive residual stresses are lower than solid ones; nevertheless, their peak tensile residual stress is higher than solid ones.

Fig. 19 illustrates the distribution of longitudinal stress in (B–B). Both elements show compressive residual stress on the inner surface and tensile residual stress on the outer surface. The distribution form shows that the solid and shell elements have similarities at x = 4 mm, 20 mm,

50 mm. However, at x = 0.7 mm they differ in distribution form. At x = 0.7 mm. The shell element is significantly higher than the solid element at the inner and outer surfaces, representing peak compressive and tensile residual stress, respectively. For longitudinal residual stress distribution at x = 4 mm, 20 mm, 50 mm, similar distribution form for both elements. The inner surface contains compression stresses, and the outer is tensile. The ultimate compressive residual stress has existed above the mid surface for both elements. Maximum residual tensile stress exists below the mid-surface for the shell element and at the mid surface for the solid element. Shell peak compressive residual stresses are lower than solid ones, but their peak tensile residual stress is higher than solid ones.

Fig. 20 illustrates the longitudinal stress distribution at the curve's end (C–C). Both elements show compressive residual stress on the inner surface and tensile residual stress at the outer surface. The distribution form shows that the solid and shell elements have similarities at x = 4 mm, 20 mm, 50 mm. However, at x = 0.7 mm they differ in distribution form. At x = 0.7 mm, shell element has a zig-zag distribution. They approach peak compressive and tensile residual stress at inner and outer surfaces. For longitudinal residual stress distribution at x = 4 mm, 20 mm, 50 mm, similar distribution form for both elements. The inner surface contains compression stresses and the outer is tensile. At x = 4 mm, both elements reach their peak compressive residual stress above
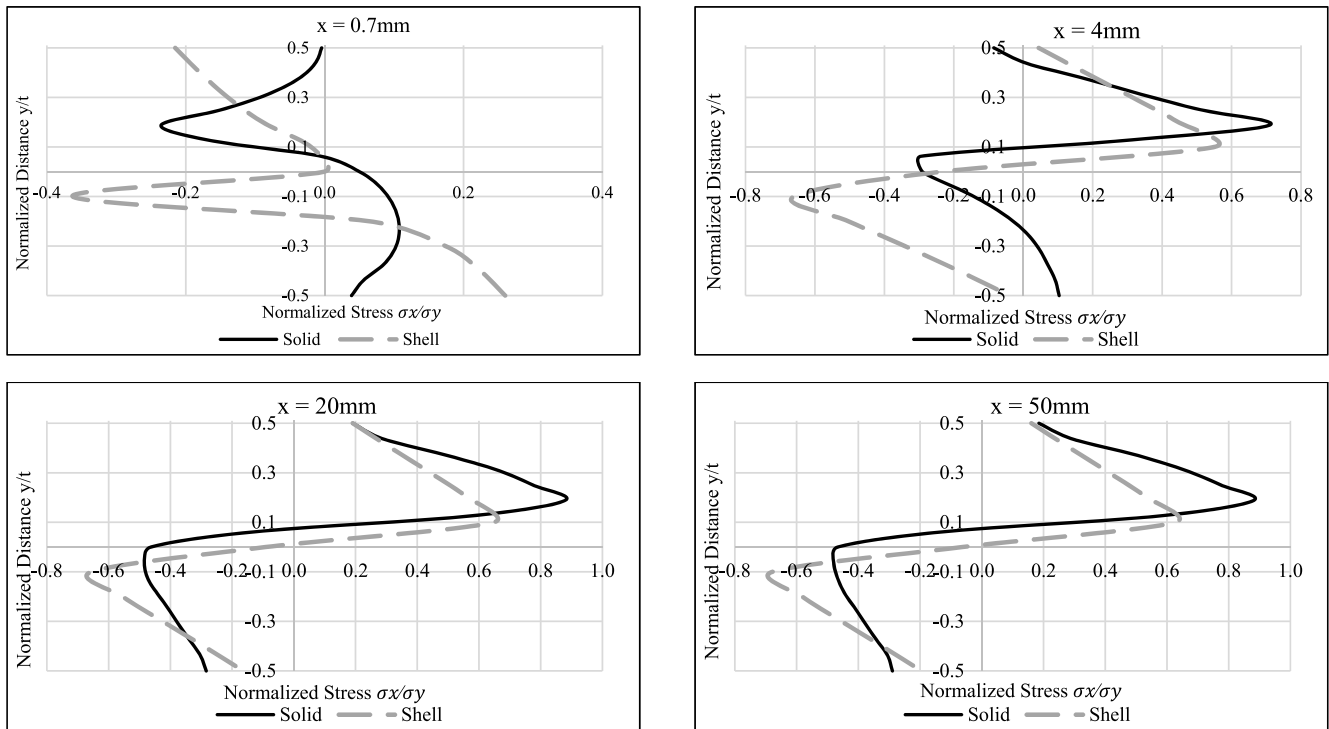
Fig. 18. Variation of longitudinal residual stresses' variation of a PBC14 section in (A–A) compared to 3D-Solid FE.
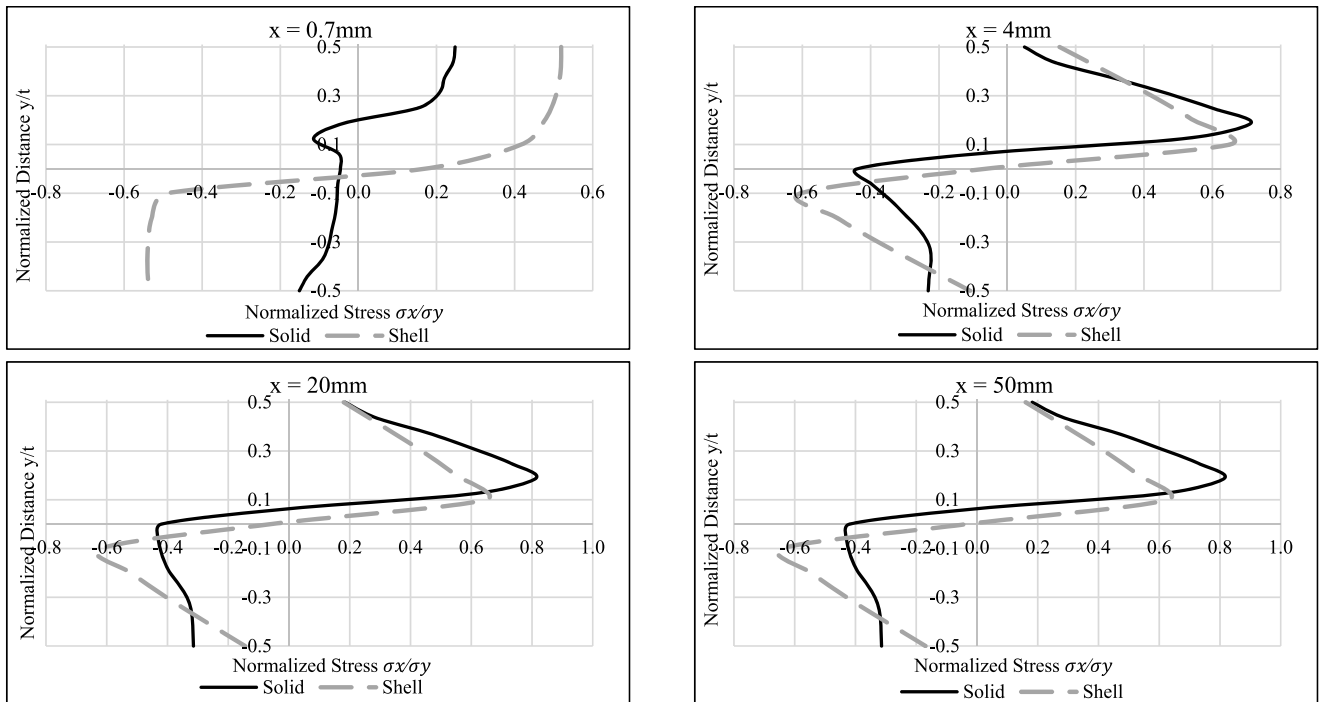

Fig. 19. Variation of longitudinal residual stresses' variation of a PBC14 section in (B–B) compared to 3D-Solid FE.

the mid-surface, although the solid element is higher than the shell element. For tensile residual stress, the solid element approaches it slightly above the mid-surface, whereas the shell element approaches it below the mid-surface. For longitudinal residual stress distribution at x = 20 mm and 50 mm, there is a similar distribution form for both elements. The inner surfaces contain compression stresses and the outer surfaces are tensile. Similarly to x = 4 mm, the maximum compressive

residual stress has existed above the mid-surface for both elements. Maximum tensile residual stress has existed below the mid-surface. Generally, the maximum compressive and tensile residual stresses for shell elements are lower than those for solid elements.

3.4.2. Transverse through-thickness residual stress variation
Fig. 21 illustrates the distribution of transverse stress at mid-corner
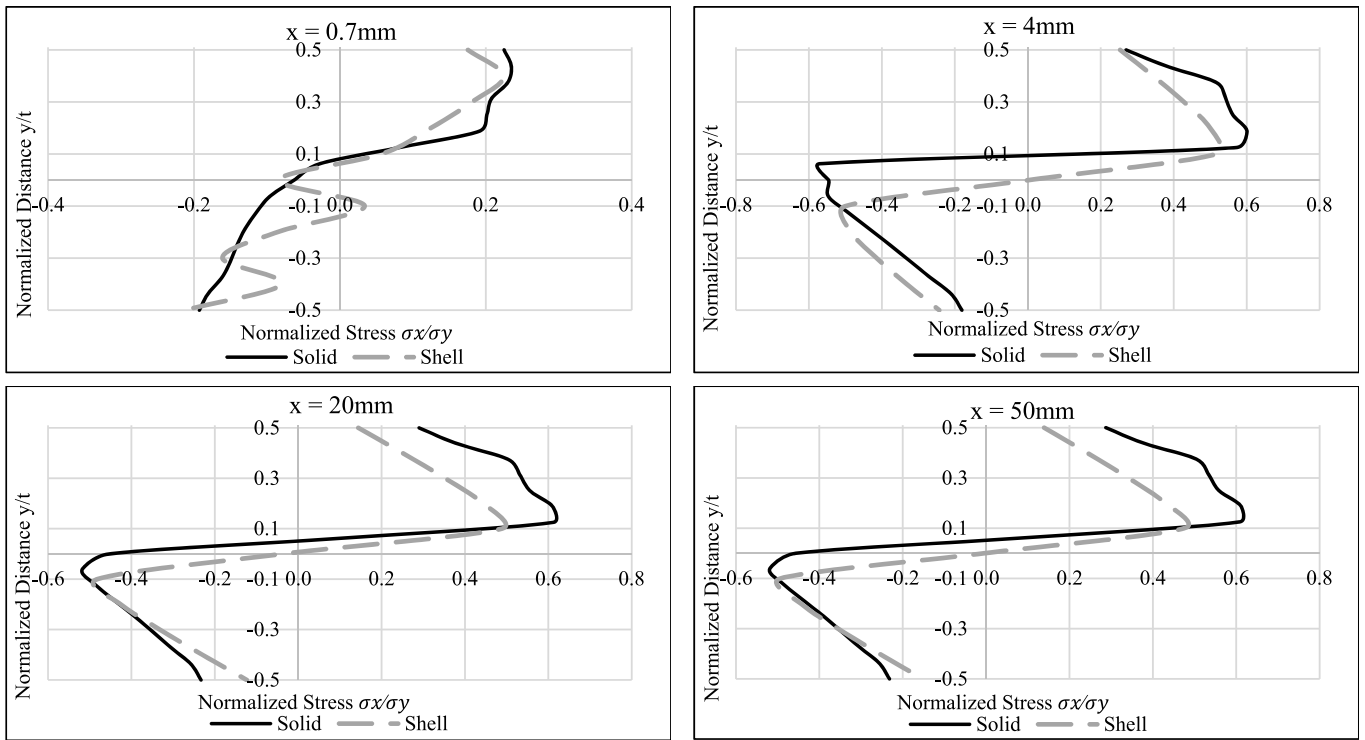
Fig. 20. Variation of longitudinal residual stresses' variation of a PBC14 section in (C–C) compared to 3D-Solid FE.
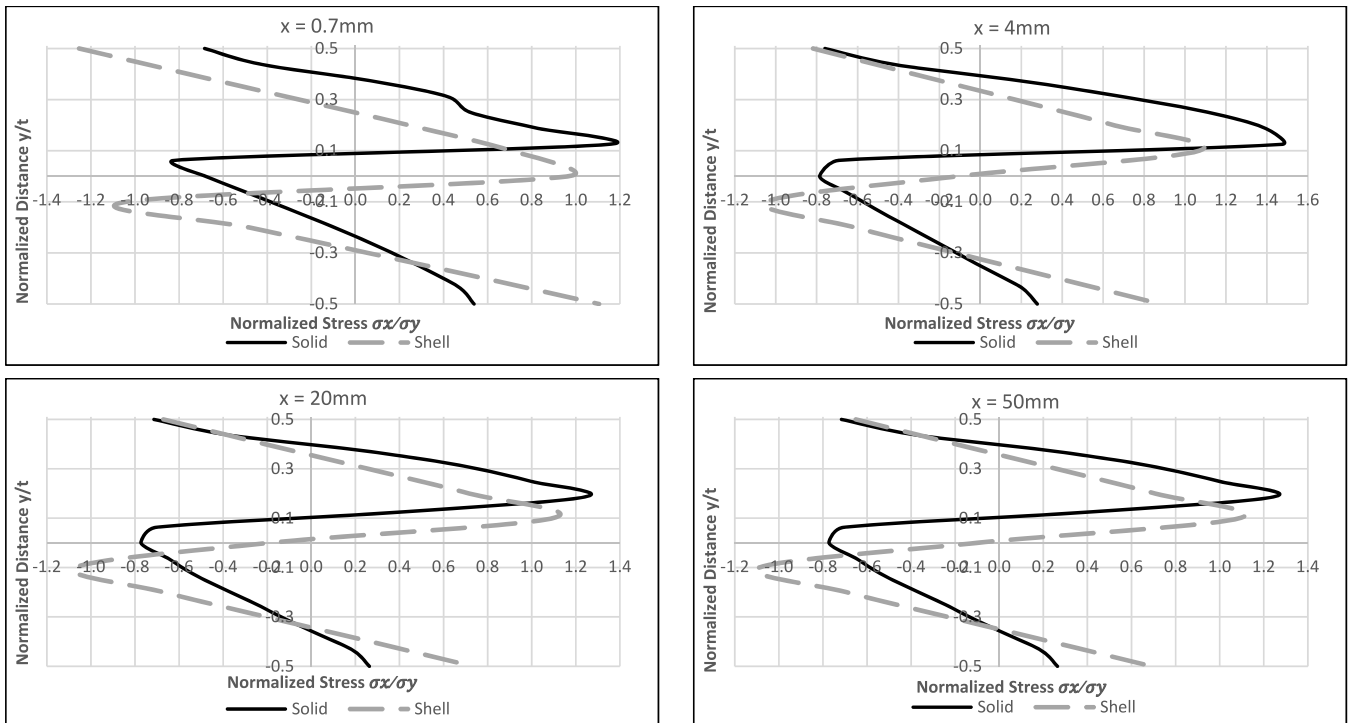

Fig. 21. Through-thickness transverse residual stresses' variation of a PBC14 section at (A–A) compared to 3D-Solid FE.

(A-A). The distribution pattern shows that the solid element and the shell element have similarities: tensile at the inner surface and compression at the outer surface. At x = 0.7 mm, maximum residual tensile and compressive stress exists at the inner and outer surfaces, respectively. At x = 4 mm, 20 mm, 50 mm transverse stress showed a linear distribution form along the middle corner (A-A) for each element.

Peak compressive residual stress for shell elements is less than solid elements while vice versa for peak tensile residual stress. These peak compressive residual stresses have existed above mid-surface for solid and shell elements. Peak tensile residual stresses exist beneath the mid-surface for the shell element, but they are at the mid-surface for the solid element.
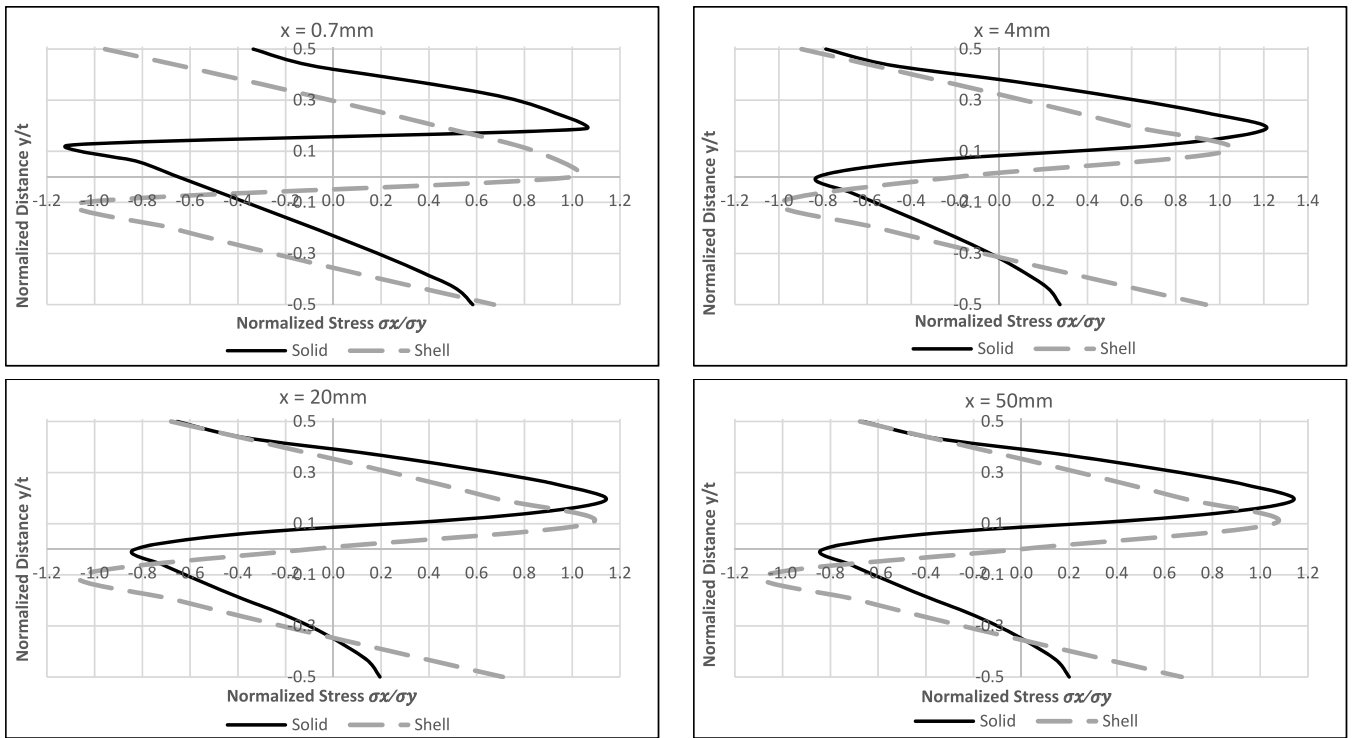
Fig. 22. Through-thickness transverse residual stresses' variation of a PBC14 section at (B–B) compared to 3D-Solid FE.

Fig. 22 demonstrates the distribution of transverse stress in the middle of the curve (B–B). The distribution form shows that the solid element and the shell element have similarities, in that it is tensile at the inner surface and compression at the outer surface. At x = 0.7 mm, the shell element maximum compressive residual stress exists at mid-surface while it is above it for solid element. Furthermore, the residual stress peaks below the mid-surface for shell element and above it once for solid. At x = 4 mm, 20 mm, 50 mm transverse stress showed a linear distribution along (B–B) for each element. Peak compressive residual stress for shell elements is less than for solid elements, while vice versa for peak tensile residual stress. These peak compressive residual stresses have existed above the mid-surface for solid and shell elements. Peak
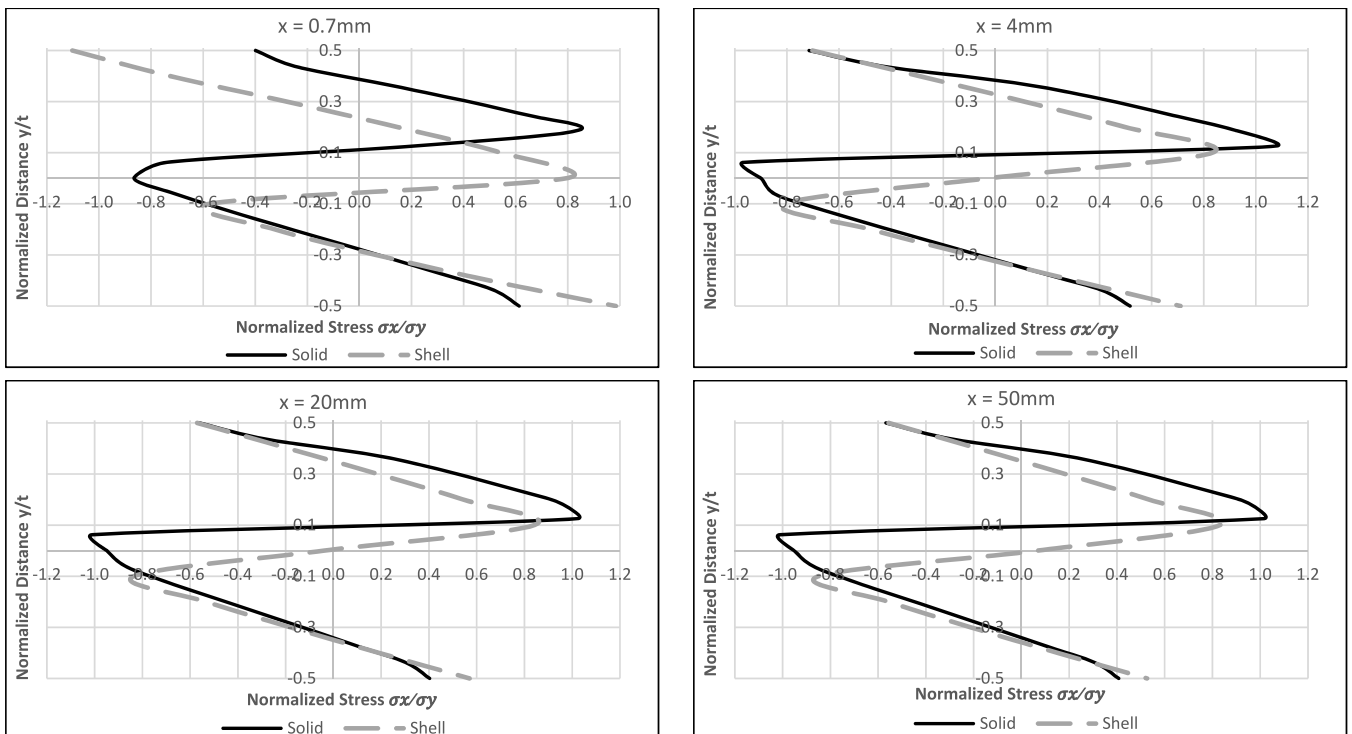

Fig. 23. Through-thickness transverse residual stresses' variation of a PBC14 section at (B–B) compared to 3D-Solid FE.
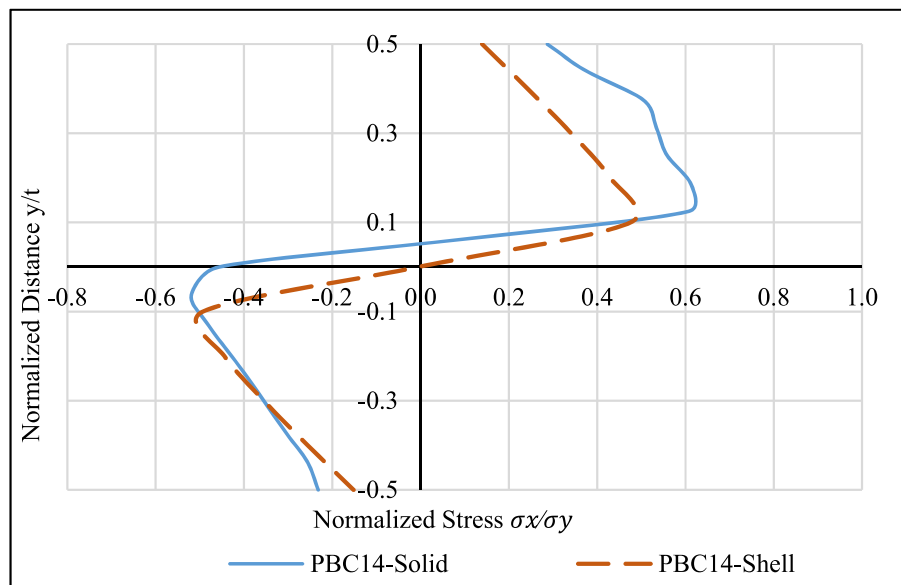
Fig. 24. Neutral axis shift for 3D-solid and 3D-Shell FE at x = 50 mm (Specimen PBC14).

tensile residual stresses exist beneath the mid-surface for the shell element, but they are at the mid-surface for the solid element.

Fig. 23 shows the distribution of transverse stress at end-corner (C–C). The distribution form shows that the solid element and the shell element have similarities, in that it is tensile at the inner surface and compression at the outer surface. At x = 0.7 mm, the shell's maximum tensile and compressive residual stress exists at the inner and outer surfaces respectively. However, solid maximum compressive residual stresses exist above mid-surface and tensile residual stresses exiting at mid-surface. At x = 4 mm, 20 mm, 50 mm transverse stress showed a linear distribution (C–C) for each element. The maximum tensile and compressive residual stresses for the shell element is less than those for the solid elements. These peak compressive residual stresses have existed above mid-surface for solid and shell elements. Peak tensile residual stresses exist beneath the shell element's mid-surface but are also above the solid element's mid-surface.

3.5. Neutral axis shift

The press braking process is bending, in which the plate is bent to a certain shape. This bending process results in the material reaching its plastic form. Thickness reduction and neutral axis shift have resulted from this process. Neutral axis shifting (NAS) is essential during bending, characterizing tension compression through the plate thickness. Many studies recently described (NAS) tube bending, such as [27, 54–57]. Also, for roll-forming, Traub et al., 2017 [58]. Cook, 1966 [59], noted that the neutral axis is shifted toward the compressive face of the plate by around 5 % in plastic bending operations. Johnson, 1980 [60] also gave an empirical formulation relevant for bend angles exceeding 70° and width to thickness ratios of more than 10. This formula considers the neutral axis shift by around 5 % toward the compressive face. This section discusses the ability of the shell and solid elements to predict the neutral axis shift (NAS) for longitudinal residual stresses during press-braking.

Fig. 24, shows longitudinal residual stress distribution for PBC14 specimen at mid-plate (x = 50 mm). The solid element shows a shift in the neural axis greater than 10 % of the plate thickness. The NAS of the PBC14 specimen exceeded 7.5 % of the plate thickness. Conversely, the shell element did not show any significant neutral shift for the specimen. The difference in the shift ratio in the solid element could be attributed to the effect of geometric and material aspects. However, it seems no contribution from these aspects in the shell element.

4. Conclusion

This study examined the prediction of residual stress distribution in press-braked thin-walled cold-formed steel sections using the 3D-Shell finite element (FE) technique. Residual stresses, which are generated during cold-forming processes, significantly impact the structural capacity of these sections. Previous research has primarily relied on the 3D-Solid FE technique for predicting through-thickness residual stresses. Although researchers explained 3D-Shell element in predicting through-thickness residual stresses, other researchers recommended it as an effective element to predict through-thickness residual stress. Consequently, this study aimed to compare the longitudinal/transverse residual stresses and neutral axis displacement obtained through the 3D-Shell FE technique with findings reported in the literature using the 3D-Solid FE technique. By conducting these comparisons, this research offers novel insights into the predictive capabilities and potential benefits of employing the 3D-Shell FE technique in analyzing the distribution of residual stresses in thin-walled cold-formed steel sections. However, the following points were highlighted as the main conclusions:

The longitudinal residual strain at inner/outer surfaces using 3D-Shell FE can be predicted as effective as the 3D-Solid FE approach. Both elements obtained closer residual strains to the experiment.

➢ The 3D-Shell element exhibits peak tensile stresses higher than those of 3D-Solid and 2D-FE elements, while its peak compressive stresses are lower than those of 3D-Solid and 2D-FE elements.
➢ The longitudinal through-thickness residual stress variation analysis reveals distinct patterns between 3D-Solid and 3D-Shell elements at different locations along the formed section, with notable differences in peak compressive and tensile stresses. Overall, while both elements exhibit similar stress distributions at certain points, the 3D-Shell element tends to show lower maximum compressive residual stresses but higher maximum tensile residual stresses compared to 3D-Solid elements.
➢ The analysis of transverse through-thickness residual stress variation reveals consistent patterns between 3D-Solid and 3D-Shell elements, with both exhibiting tensile stresses at the inner surface and compressive stresses at the outer surface. Notably, peak compressive residual stresses are lower in 3D-Shell elements compared to 3D-Solid elements, while vice versa for peak tensile residual stresses. These findings are consistent across different locations along the

formed section, indicating a robust pattern of stress distribution in both element types.

➢ Longitudinal residual stresses in the flat region do not follow the corner region, exhibiting tensile stress on the top surface and compressive stress on the bottom surface, with maximum values near the edge's corner region. On the other hand, transverse residual stresses in the flat region follow the corner region.

➢ The 3D-Solid FE technique can predict neutral axis shifting due to bending. This shifting changes concerning the geometric and material aspects. Although the 3D-Shell FE technique can vary the residual stress variation, it does not predict neutral axis shifting.

CRediT authorship contribution statement

Ayad Mutafi: Conceptualization, Formal analysis, Methodology, Software, Writing – original draft. **J.M. Irwan:** Supervision, Writing – review & editing. **Noorfaizal Yidris:** Supervision. **Atef M. Ghaleb:** Supervision. **Sami Al-Alimi:** Formal analysis. **Mugahed Amran:** Writing – review & editing. **Maged Qasem:** Formal analysis, Software. **Mousa Hasan:** Validation. **Amin Al-Fakih:** Methodology.

Declaration of competing interest

The authors declare that they have no known competing financial interests or personal relationships that could have appeared to influence the work reported in this paper.

Data availability

Data will be made available on request.

References

[1] M.A. Ablat, A. Qattawi, Numerical simulation of sheet metal forming: a review. The international journal of advanced manufacturing technology 89 (1) (2017) 1235–1250.

[2] A. Makinouchi, Sheet metal forming simulation in industry. Journal of Materials Processing Technology 60 (1–4) (1996) 19–26.

[3] M.J. Finn, et al., Use of a coupled explicit-implicit solver for calculating springback in automotive body panels. Journal of Materials Processing Tech 50 (1–4) (1995) 395–409.

[4] W.M. Quach, J.G. Teng, K.F. Chung, Finite element predictions of residual stresses in press-braked thin-walled steel sections, Eng. Struct. 28 (11) (2006) 1609–1619.

[5] J.-z. Liu, H. Fang, T.-M. Chan, Investigations on material properties and residual stresses in cold-formed high strength steel irregular hexagonal hollow sections, Thin-Walled Struct. 176 (2022) 109220.

[6] A. Abvabi, et al., An inverse routine to predict residual stress in sheet material, Mater. Sci. Eng., A 652 (2016) 99–104.

[7] C.C. Weng, R.N. White, Residual stresses in cold-bent thick steel plates, J. Struct. Eng. 116 (1) (1990) 24–39.

[8] C.C. Weng, P.T., Residual stresses in cold-formed steel members, J. Struct. Eng. 116 (6) (1990) 1611–1625.

[9] M.C. Lee, et al., Three-dimensional simulation of forging using tetrahedral and hexahedral elements. Finite Elements in Analysis and Design 45 (11) (2009) 745–754.

[10] W. Chung, et al., Finite element simulation of plate or sheet metal forming processes using tetrahedral MINI-elements, J. Mech. Sci. Technol. 28 (1) (2014) 237–243.

[11] L.F. Menezes, C. Teodosiu, Three-dimensional numerical simulation of the deep-drawing process using solid finite elements, J. Mater. Process. Technol. 97 (1) (2000) 100–106.

[12] Y. Sun, et al., Predictive modelling of longitudinal bow in Chain-die formed AHSS profiles and its experimental verification, J. Manuf. Process. 39 (2019) 208–225.

[13] M. Sun, J.A. Packer, Hot-dip galvanizing of cold-formed steel hollow sections: a state-of-the-art review, Front. Struct. Civ. Eng. 13 (1) (2019) 49–65.

[14] Y. Li, et al., A numerical study on chain-die forming of the AHSS U-channel and contrast with roll forming, Int. J. Mech. Sci. 135 (2018) 279–293.

[15] Y. Sun, et al., Longitudinal strain development in Chain-die forming AHSS products: analytical modelling, finite element analysis and experimental verification, J. Mater. Process. Technol. 243 (2017) 322–334.

[16] Z. Qian, et al., Experimental and numerical investigation of flange angle in Chain-die formed AHSS U-channel sections, Int. J. Adv. Des. Manuf. Technol. 92 (1) (2017) 1231–1242.

[17] A.D. Deole, M.R. Barnett, M. Weiss, The numerical prediction of ductile fracture of martensitic steel in roll forming, Int. J. Solid Struct. (2018) 20–31, 144-145.

[18] S.P. Chiew, Y.F. Jin, C.K. Lee, Residual stress distribution of roller bending of steel rectangular structural hollow sections, J. Constr. Steel Res. 119 (2016) 85–97.

[19] B. Rossi, H. Degée, R. Boman, Numerical simulation of the roll forming of thin-walled sections and evaluation of corner strength enhancement. Finite Elements in Analysis and Design 72 (2013) 13–20.

[20] M.M. Pastor, et al., Residual stresses and initial imperfections in non-linear analysis, Eng. Struct. 46 (2013) 493–507.

[21] J. Larrañaga, et al., Development and validation of a numerical model for sheet metal roll forming, Int. J. Material Form. 3 (1) (2010) 151–154.

[22] J. Paralikas, K. Salonitis, G. Chryssolouris, Investigation of the effects of main roll-forming process parameters on quality for a V-section profile from AHSS, Int. J. Adv. Des. Manuf. Technol. 44 (3) (2009) 223–237.

[23] Q.V. Bui, J.P. Ponthot, Numerical simulation of cold roll-forming processes, J. Mater. Process. Technol. 202 (1) (2008) 275–282.

[24] M. Murugesan, M. Sajjad, D.W. Jung, Experimental and numerical investigation of AA5052-H32 Al alloy with U-profile in cold roll forming, Materials 14 (2) (2021) 470.

[25] C.D.S. Souto, et al., Determination of manufacturing residual stresses in cold-formed thin-walled steel profiles, Thin-Walled Struct. 180 (2022) 109945.

[26] J. Bonada, et al., Influence of the cold work effects in perforated rack columns under pure compression load, Eng. Struct. 97 (2015) 130–139.

[27] B. Engel, H. Hassan, Advanced model for calculation of the neutral axis shifting and the wall thickness distribution in rotary draw bending processes. Int J Mech, Aerosp Ind Mechatronics Eng 9 (2) (2015) 239–243.

[28] Y. Yan, et al., A novel roll-die forming technology and its FEM simulation, Procedia Eng. 207 (2017) 1302–1307.

[29] A. Mutafi, 3D finite element technique in determining residual stresses and strains of press-braked carbon/stainless steel, Universiti Putra Malaysia (2020).

[30] A. Mutafi, et al., Investigation into the distribution of residual stresses in pressed-braked thin-walled steel lipped channel sections using the 3D-FEM technique, Thin-Walled Struct. 135 (2019) 437–445.

[31] A. Mutafi, et al., An investigation on longitudinal residual strains distribution of thin-walled press-braked cold formed steel sections using 3D FEM technique, Heliyon 4 (11) (2018) e00937 p. e00937.

[32] E.J. Gerbo, et al., Full-field measurement of residual strains in cold bent steel plates, J. Constr. Steel Res. 127 (2016) 187–203.

[33] Y. Yao, W.-M. Quach, B. Young, Finite element-based method for residual stresses and plastic strains in cold-formed steel hollow sections, Eng. Struct. 188 (2019) 24–42.

[34] Y. Yao, W.M. Quach, B. Young, Cross-section behavior of cold-formed steel elliptical hollow sections – a numerical study, Eng. Struct. (2019) 201.

[35] J. Falsafi, E. Demirci, V.V. Silberschmidt, Numerical study of strain-rate effect in cold rolls forming of steel, J. Phys. Conf. 451 (2013) 12041.

[36] X. Zhao, M. Tootkaboni, B.W. Schafer, Laser-based cross-section measurement of cold-formed steel members: model reconstruction and application, Thin-Walled Struct. 120 (2017) 70–80.

[37] R. Safdarian, H. Moslemi Naeini, The effects of forming parameters on the cold roll forming of channel section, Thin-Walled Struct. 92 (2015) 130–136.

[38] A. Mutafi, et al., 3D Fem to Predict Residual Stresses of Press-Braked Thin-Walled Steel Sections, in Lecture Notes in Civil Engineering, 2019, pp. 215–224.

[39] T. Trzepiecinski, H.G. Lemu, Effect of computational parameters on springback prediction by numerical simulation, Metals 7 (9) (2017) 380.

[40] V. Vorkov, et al., Springback prediction of high-strength steels in large radius air bending using finite element modeling approach, Procedia Eng. 81 (2014) 1005–1010.

[41] G. Zeng, et al., Optimization design of roll profiles for cold roll forming based on response surface method, Mater. Des. 30 (6) (2009) 1930–1938.

[42] F. Wang, Numerical studies of residual stress in cold formed steel sigma sections, Numerical studies of residual stress in cold formed steel sigma sections (2015).

[43] Y. Yao, W.-M. Quach, B. Young, Simplified models for residual stresses and equivalent plastic strains in cold-formed steel elliptical hollow sections, Thin-Walled Struct. 154 (2020) 106835.

[44] J.W. Cho, D.Y. Yang, W.J. Chung, A simplified approach for incorporating thickness stress in the analysis of sheet metal forming using shell elements, Int. J. Numer. Methods Eng. 53 (10) (2002) 2311–2327.

[45] M. Zhang, X. Tian, Residual stresses and strains analysis in press-braking bending parts considering multi-step forming effect, Proc. IME B J. Eng. Manufact. 234 (4) (2019) 788–800.

[46] X. Han, L. Hua, 3D FE modeling of cold rotary forging of a ring workpiece, J. Mater. Process. Technol. 209 (12) (2009) 5353–5362.

[47] I. Koutromanos, Fundamentals of Finite Element Analysis: Linear Finite Element Analysis, Wiley, 2018.

[48] W.M. Quach, J.G. Teng, K.F. Chung, Residual stresses in steel sheets due to coiling and uncoiling: a closed-form analytical solution, Eng. Struct. 26 (9) (2004) 1249–1259.

[49] R. Wagoner, M. Li, Simulation of springback: through-thickness integration, Int. J. Plast. 23 (3) (2007) 345–360.

[50] Abaqus 6.13-4, Dassault systèmes simulia corp., .Providence, RI.

[51] H. Amouzegar, B.W. Schafer, M. Tootkaboni, An incremental numerical method for calculation of residual stresses and strains in cold-formed steel members, Thin-Walled Struct. 106 (2016) 61–74.

[52] D.W. Jung, Study of dynamic explicit analysis in sheet metal forming processes using faster punch velocity and mass scaling scheme, J. Mater. Eng. Perform. 7 (4) (1998) 479–490.

[53] J. Loughlan, N. Yidris, P.R. Cunningham, The effects of local buckling and material yielding on the axial stiffness and failure of uniformly compressed I-section and box-section struts, Thin-Walled Struct. 49 (2) (2011) 264–279.

[54] H. Li, et al., An insight into neutral layer shifting in tube bending, Int. J. Mach. Tool Manufact. 126 (2018) 51–70.

[55] B. Liu, et al., Analytical model of neutral layer shift in tube bending introducing material parameters, Hangkong Xuebao/Acta Aeronautica et Astronautica Sinica 37 (3) (2016) 1074–1082.

[56] B. Engel, H.R. Hassan, Investigation of neutral axis shifting in rotary draw bending processes for tubes, Steel Res. Int. 85 (7) (2014) 1209–1214.

[57] E, D., X. Guo, and R. Ning, Analysis of strain neutral layer displacement in tube-bending process, Jixie Gongcheng Xuebao/Journal of Mechanical Engineering 45 (3) (2009) 307–310.

[58] T. Traub, X. Chen, P. Groche, Experimental and numerical investigation of the bending zone in roll forming, Int. J. Mech. Sci. (2017) 956–970, 131-132.

[59] N.H. Cook, Manufacturing Analysis, Addison-Wesley Co., Reading, MA, 1966.

[60] W. Johnson, P.B. Mellor, Engineering Plasticity, Van Nostrand Reinhold New York, NY, 1980.